Spring 1-1-2017

Bifidelity Methods for Polynomial Chaos Expansions

Michaela Farr
University of Colorado at Boulder, farrmg@colorado.edu

Bifidelity Methods for Polynomial Chaos Expansions

by

Ms. Michaela Farr

B.S., University of New Mexico, 2013

A thesis submitted to the

Faculty of the Graduate School of the

University of Colorado in partial fulfillment

of the requirements for the degree of

Master of Science

Department of Mechanical Engineering

2017

This thesis entitled:
Bifidelity Methods for Polynomial Chaos Expansions
written by Ms. Michaela Farr
has been approved for the Department of Mechanical Engineering

Prof. Alireza Doostan

Prof. Daven Henze

Prof. Peter Hamlington

Date _____

The final copy of this thesis has been examined by the signatories, and we find that both the content and the form meet acceptable presentation standards of scholarly work in the above mentioned discipline.

Michaela Farr, Ms. (M.S. Mechanical Engineering)

Bifidelity Methods for Polynomial Chaos Expansions

Thesis directed by Prof. Alireza Doostan

This thesis provides an in-depth evaluation of two multi fidelity uncertainty quantification techniques, highlighting the key characteristics, benefits, and shortcomings therein. Physics based simulations subject to uncertain inputs are used to demonstrate the efficacy of each technique in reducing the computational cost of generating a polynomial chaos (PC) approximation of a simulated quantity of interest(QoI). Considered is a weighted ℓ_1 minimization technique, wherein a priori estimates on the decay of PC coefficients are used to generate sparse PC approximations of the QoI. Also considered is a stochastic basis reduction method, which identifies a subspace that spans the PC basis by principle component analysis of the covariance of the QoI. Numerical tests were conducted upon 2 airfoil simulations subject to 6 uncertain inputs (one at high Mach number, one at low) and a lithium ion battery simulation subject to 17 uncertain inputs to evaluate each method. The examples studied illustrate the main characteristics of each method and provide insight to their applicability to UQ in numerical simulations. Appreciable reductions in computational resources were observed in all cases when compared to direct simulation of a high fidelity model.

Acknowledgements

I would like to thank my adviser, Alireza Doostan, for his guidance, support, and patience throughout my Master's program. I would like to acknowledge the members of my committee: Daven Henze and Peter Hamlington for their feedback, suggestions, and help. Thank you, my colleague and friend Matthew Lawry, for your unwavering support during this process. Mom, thank you for giving me the gift of tenacity and Sophie, thank you for being such a bright light in my life. Finally, thank you Dad for inspiring my love of science and reminding me to always carry the fire. I dedicate this thesis to you.

Contents

Chapter

1 Introduction **1**

1.1 Uncertainty Quantification in Computational Sciences 1

1.2 Polynomial Chaos 2

1.3 Mathematical Formulation of the PCE 2

1.3.1 Convergence properties 4

1.4 Solving for the coefficients 5

1.4.1 Sampling methods - Least squares regression 7

1.4.2 Sampling methods - Compressive sensing 8

1.4.3 Sampling methods - Spectral Projection 9

1.5 Motivation 11

1.5.1 Contributions of this thesis 11

1.5.2 Bi fidelity weighted ℓ_1 minimization 12

1.5.3 Bi fidelity stochastic basis reduction 12

2 Weighted L1 Minimization **14**

2.1 Introduction 14

2.2 Compressive Sensing 14

2.3 Weighted BPDN 16

2.4 Multi fidelity WBPDN 18

2.5 Test Problems . . . 19
2.6 NACA0012 airfoil . . . 19
2.6.1 Mach number M . . . 19
2.6.2 Angle of attack α . . . 20
2.6.3 Geometrical Parameters . . . 20
2.7 Numerical Tests . . . 21
2.7.1 Metrics . . . 23
2.7.2 Results . . . 24
2.8 Lithium Ion Battery Model . . . 25
2.8.1 Porosity ϵ . . . 26
2.8.2 Bruggeman coefficient, brugg . . . 26
2.8.3 LI^+ transference number, t_+^0 . . . 27
2.8.4 Diffusion coefficients, D and D_s . . . 27
2.8.5 Electronic conductivities, σ and σ_s . . . 27
2.8.6 Reaction rate constant k . . . 28
2.8.7 Additional parameters . . . 28
2.9 Numerical tests . . . 29
2.10 Discussion . . . 30

3 Stochastic Reduced Basis Method **34**

3.1 Introduction . . . 34
3.2 Model Reduction . . . 34
3.3 Karhunen - Loeve Expansion . . . 35
3.4 Projection onto the PCE basis . . . 36
3.5 Numerical Tests . . . 38
3.5.1 Airfoil Results . . . 39
3.5.2 LIB Results . . . 40

3.6 Discussion 40

4 Conclusion **45**

4.1 Summary 45

4.2 Future Work 47

Bibliography **49**

Appendix

.1 Determination of δ 55

Tables

Table

1.1 Wiener-Askey polynomial chaos with corresponding probability distributions [85]. . . 5

2.1 List of random airfoil inputs used in this study. 22

2.2 List of random LIB inputs used in this study. 29

3.1 Table of relative error in eigenvalue data as a function of rank r. 39

Figures

Figure

1.1 (a) The first 5 Hermite polynomials and the (b) Gaussian Distribution. 6

1.2 (a) The first 5 Legendre polynomials and the (b) Uniform distribution. 7

2.1 A comparison of the different ℓ_p norms of $\boldsymbol{c}$ in three dimensions. 16

2.2 Recovery of a sparse $\boldsymbol{c}_0$ via standard and weighted ℓ_1 minimization. (a) The signal, $\boldsymbol{c}_0 \in \mathbb{R}^3$ has a sparsity of 1 (i.e., has one non-zero entry) and therefor exists as a point on one of the axes of the ℓ_1 ball. Assuming our system is under-determined, ($\boldsymbol{u}$ contains two or fewer measurements) $\boldsymbol{\Psi}$ has a nullity of 1 (represented by the red line). Any point along this line satisfies $\boldsymbol{\Psi C} = \boldsymbol{U}$. It can be seen in (b) that there exists $\boldsymbol{c} \neq \boldsymbol{c_0}$ for which $\|\boldsymbol{c}\|_1 < \|\boldsymbol{c_0}\|_1$, resulting in the algorithm returning a non-sparse $\boldsymbol{c}$. Weighting the ℓ_1 term, as in (c), reduces the size of the solution space, enforcing $\boldsymbol{c} \neq \boldsymbol{c_0}$ for all $\|\boldsymbol{Wc}\|_1 < \|\boldsymbol{Wc_0}\|_1$, and thereby increasing the likelihood of returning a sparse $\boldsymbol{c}$. 17

2.3 NACA0012 airfoil parameters. 21

2.4 (a) A sample mean profile for $N^H = 10$ for airfoil Test 1 alongside (b) a close up of mean for airfoil Test 1. 23

2.5 (a) A sample mean profile for $N^H = 10$ alongside (b) a close up of the mean for airfoil Test 2. 24

2.6 (a) A sample variance profile for $N^H = 10$ alongside (b) a close up of the variance for airfoil Test 1. 25

2.7 (a) A sample variance profile for $N^H = 10$ alongside (b) a close up of the variance for airfoil Test 2. 26

2.8 (a) The average of the normalized error of the mean of err_μ and (b) the variance of err_μ for airfoil Test 1. 27

2.9 (a) The average of the normalized error of the mean of err_μ and (b) the variance of err_μ for airfoil Test 2. 28

2.10 (a) The average of the normalized error of the variance of err_{σ^2} and (b) the variance of err_{σ^2} for airfoil Test 1. 29

2.11 (a) The average of the normalized error of the variance of err_{σ^2}, and (b) the variance of err_{σ^2} for airfoil Test 2. 30

2.12 LIB schematic. Image taken courtesy of [47]. 32

2.13 (a) A sample of the mean and (b) variance profiles as predicted by u^H ($N_H = 30$), u^L, u^{Bi}, and u^{Ref} for the LIB model. 32

2.14 (a) The average of the mean error and (b) the variance of the mean error for LIB model. 33

2.15 (a) The average of the variance error and (b) the variance of the variance error for LIB model. 33

3.1 (a) The average of the error of the mean and (b) the variance of the error of the mean for airfoil Test 1. 40

3.2 (a) the average of the error of the mean (b) the variance of the mean error for airfoil Test 2. 41

3.3 (a) The mean variance and (b) the variance of the variance for airfoil Test 1. 42

3.4 (a) The average of the error of the variance and (b) the variance of the variance for airfoil Test 2. 42

3.5 (a) The average error of the mean and (b) the variation of the error of the mean for LIB model. 43

3.6 (a) The average error of the variance and (b) the variance of the error in predicted variance for LIB model. 43

3.7 (a) Normalized eigenvalues for airfoil Test 1 (b) and airfoil Test 2. 44

3.8 Normalized Eigenvalues of the LIB model for $N^H = 30$. 44

1 Study of δ_w using lower dimensional stochastic airfoil model. 56

Chapter 1

Introduction

1.1 Uncertainty Quantification in Computational Sciences

Our ability to simulate complex physical phenomena has sky-rocketed with the advent of modern computational resources. Simulations are an essential decision making tool for many fields of engineering. As modeling capabilities expand, it becomes increasingly important to rigorously identify the limitations and uncertainties associated with these models so that they are treated neither with unfounded confidence nor skepticism. The uncertainties inherent in a simulated representation of a quantity of interest (QoI) may be classified into two broad categories: epistemic and aleatory. Epistemic uncertainty originates from an imperfect knowledge or representation of the underlying physics of the system and may be non-trivial to quantify or alleviate. On the contrary, aleatory uncertainties, which arise from intrinsic systemic variabilities, may be identified using well established probabilistic techniques. Material properties such as Young's modulus or viscosity, or slight geometrical variations in the design of an airfoil, may be treated as aleatory uncertainties. Statistical inputs into a given partial differential equation (PDE) solver impart probabilistic character to would-be deterministic outputs, so that they are best represented by moments, probability of failure analysis, or probability density functions (pdf). Uncertainty quantification aims to characterize this relationship between parameter uncertainties and predicted response behaviour, specifically for computational models.

1.2 Polynomial Chaos

The polynomial characterization of random physical behaviour has garnered much interest within the UQ community. Seminally introduced by N. Wiener in 1938 [83], a summation of orthogonal Hermite polynomials was used as a means of representing a Gaussian stochastic process. It was later shown that such expansions yield universal L_2 convergence to any process with finite second order moments [38], an appropriate assumption given that most random physical processes have finite variance. This polynomial expansion technique was subsequently generalized to include functionals of other common distributions [4], as well as for distributions of arbitrary form. This general class of methods is known as Polynomial Chaos (PC). Polynomial Chaos Expansions (PCEs) have been utilized extensively for engineering applications as well as in other scientific facets such as birth-death analysis [55] and in the integration theory of Brownian motion [83]. Ghanem and Spanos successfully used PC methods to model uncertainty in various solid mechanics problems solved using the finite element method [45, 46, 44, 43]. PC has also been implemented for modeling uncertainty in fluids problems [87, 61, 58, 73] and shows great promise for performing optimization under uncertainty [77, 90, 57].

1.3 Mathematical Formulation of the PCE

We can define a spectral representation of the QoI, u, as an infinite summation of multivariate PC basis functionals:

$$u(\boldsymbol{\xi}) = \sum_{j=1}^{\infty} c_j \psi_j(\boldsymbol{\xi}) \tag{1.1}$$

where $\boldsymbol{\xi} = (\xi_1, \cdots, \xi_d)$ is a set of independent random variables, each with probability measure $\rho(\xi_k)$, characterizing the input uncertainty, e.g., in material properties, boundary conditions, etc. In order to represent the QoI in this form, $\boldsymbol{c} = (c_1, c_2, \cdots)$, which are deterministic coefficients, must be calculated. The multivariate PC basis, denoted by $\psi_j(\boldsymbol{\xi})$, is generated from tensor products

of univariate polynomials $\psi_{j_k}(\xi_k)$ of degree j_k

$$\psi_j(\boldsymbol{\xi}) = \prod_{k=1}^{d} \psi_{j_k}(\xi_k). \tag{1.2}$$

The univariate polynomials themselves, $\psi_{j_k}(\xi_k)$, are orthogonal with respect to their probability measure, $\rho(\xi_k)$, such that

$$\langle \psi_{i_k}, \psi_{j_k} \rangle = \int_\Omega \psi_{i_k}(\xi_k)\psi_{j_k}(\xi_k)\rho(\xi_k)d\xi_k = \delta_{i_k j_k} \left\langle \psi_{i_k}^2 \right\rangle \tag{1.3}$$

where δ is the Kronecker delta and $\langle \cdot \rangle$ is the expectation operator. Due to the independence of ξ_k, the basis functionals $\psi(\boldsymbol{\xi})$ are also orthogonal i.e., $\langle \psi_i(\boldsymbol{\xi})\psi_j(\boldsymbol{\xi}) \rangle = \delta_{i,j} \left\langle \psi_i^2 \right\rangle$. Several important properties of the tensorized polynomials can be derived from their orthogonality. The first polynomial in the summation, ψ_1, also known as the degree zero polynomial is always equal to 1. It follows that

$$\langle \psi_1(\boldsymbol{\xi}) \rangle = \int_\Omega \psi_1(\boldsymbol{\xi})\rho(\boldsymbol{\xi})d\boldsymbol{\xi} = \int_\Omega \rho(\boldsymbol{\xi})d\boldsymbol{\xi} = 1. \tag{1.4}$$

For ψ_j where $j > 1$, it can be shown that

$$\langle \psi_j(\boldsymbol{\xi}) \rangle = \int_\Omega 1 \cdot \psi_j(\boldsymbol{\xi})\rho(\boldsymbol{\xi})d\boldsymbol{\xi} = \int_\Omega \psi_1(\boldsymbol{\xi})\psi_j(\boldsymbol{\xi})\rho(\boldsymbol{\xi})d\boldsymbol{\xi} = 0. \tag{1.5}$$

We can also show the variance to be

$$\mathrm{Var}(\psi_j(\boldsymbol{\xi})) = \left\langle \psi_j^2(\boldsymbol{\xi}) \right\rangle - \left(\underbrace{\langle \psi_j(\boldsymbol{\xi}) \rangle}_{0} \right)^2 = \int_\Omega \psi_j^2(\boldsymbol{\xi})\rho(\boldsymbol{\xi})d\boldsymbol{\xi} \tag{1.6}$$

where $\mathrm{Var}(\psi_1) = 0$. For orthonormal polynomials, Equation (1.6) = 1. For many applications, the uncertainty of the QoI may be adequately captured by the mean and variance alone. Higher order moments can be evaluated, for instance, by quadrature approximations of integrals [67]. The particular polynomial form of ψ_j is related to the probability density functions (pdf) of the random inputs they sample from, denoted by $\rho(\xi_k)$.

In practice, it is necessary to truncate PCE's to a finite number of terms. An expansion can be pared down in a number of ways, but the most straightforward truncation is by highest total order of polynomial P. In total order truncation, only those terms in the tensor-products of the

1D basis whose total order is less than p, i.e., $\sum_{k=1}^{d} j_k \leq p$, are retained. The total number P of basis functions of order less than p in stochastic dimension d is

$$P = \frac{(p+d)!}{p!d!}, \tag{1.7}$$

which results in an expansion of the form:

$$\hat{u}(\boldsymbol{\xi}) = \sum_{j=1}^{P} c_j \psi_j(\boldsymbol{\xi}). \tag{1.8}$$

In this form the problem of approximating the QoI essentially reduces to the problem of identifying the PC coefficients c_j.

Using the truncated PCE we can easily generate important statistics of the QoI such as the mean and variance [18]. The mean of Eq. (1.8) is given by:

$$\langle \hat{u}(\boldsymbol{\xi}) \rangle = \left\langle \sum_{j=1}^{P} c_j \psi_j(\boldsymbol{\xi}) \right\rangle = \sum_{j=1}^{P} c_j \left\langle \psi_j(\boldsymbol{\xi}) \right\rangle .$$

As $\langle \psi_j \rangle = 0$ for $j > 1$, and 1 otherwise from Equation (1.5), this results in

$$\langle \hat{u}(\boldsymbol{\xi}) \rangle = c_1. \tag{1.9}$$

By similar reasoning, one can derive an expression for the variance:

$$\mathrm{Var}\left(\hat{u}(\boldsymbol{\xi})\right) = \left\langle \sum_{j=1}^{P} c_j^2 \psi_j^2(\boldsymbol{\xi}) \right\rangle - \left\langle \sum_{j=1}^{P} c_j \psi_j(\boldsymbol{\xi}) \right\rangle^2 =$$

$$\sum_{j=1}^{P} c_j^2 \left\langle \psi_j^2(\boldsymbol{\xi}) \right\rangle - c_1^2 = \sum_{j=2}^{P} c_j^2 \left\langle \psi_j^2(\boldsymbol{\xi}) \right\rangle = \sum_{j=2}^{P} c_j^2, \tag{1.10}$$

which follows from Equation (1.6). With the appropriate choice of PC basis, and for a sufficiently smooth $\hat{u}(\boldsymbol{\xi})$ (i.e., $\hat{u}$ contains no discontinuities or severe gradients w.r.t. ξ), a PC expansion converges to a finite variance u in the mean-square sense as $p \to \infty$.

1.3.1 Convergence properties

It has been demonstrated that the convergence rate of Hermite chaos expansions is optimal and in fact exponential for Gaussian processes [59]. Hermite polynomials often exhibit poor convergence rates when they are used to approximate non-Gaussian processes however. This inspired the

$\rho(\xi_k)$	Polynomial Type	support
Gaussian	Hermite	$(-\infty, +\infty)$
Gamma	Laguerre	$(0, +\infty)$
Beta	Jacobi	[a,b]
Uniform	Legendre	[a,b]

Table 1.1: Wiener-Askey polynomial chaos with corresponding probability distributions [85].

generalization of the technique to polynomial functionals of other distributions [4] known as Wiener-Askey polynomials. In [86] the convergence rate for a handful of the Wiener-Askey polynomials was demonstrated for stochastic processes having exact solutions. Several of the Wiener-Askey polynomials, including the Hermite and Legendre polynomials, are given in Table 1.1 alongside their supports. Fig. 1.1 and Fig. 1.2 show the first few polynomials for the Hermite and Legendre bases, respectively, along with their corresponding pdfs. Generalized PCE (gPCE) further extended these concepts to distributions of arbitrary structure, as in the case where the analytical form of the distribution is unknown, or is not included in the Wiener-Askey scheme. In this case, orthogonal polynomials can be constructed numerically to deal with arbitrary probability measure [86, 80].

1.4 Solving for the coefficients

The main challenge in using the PCE lies in determining the coefficients of the expansion, $\boldsymbol{c}$. $\boldsymbol{c}$, may be computed either "intrusively", via Galerkin projection [46], or "non-intrusively", via sampling based methods. As the name implies, intrusive PC usually requires modifications of the original deterministic solvers, a task which may be infeasible either due to the inaccessibility of the numerical solvers, as in the case of legacy codes, or due to the mathematical complexity of rewriting governing equations. Non-intrusive PC is often more appealing; it treats a deterministic solver as a black box for which N samples of the random inputs $\boldsymbol{\xi}$ are used to generate realizations of the

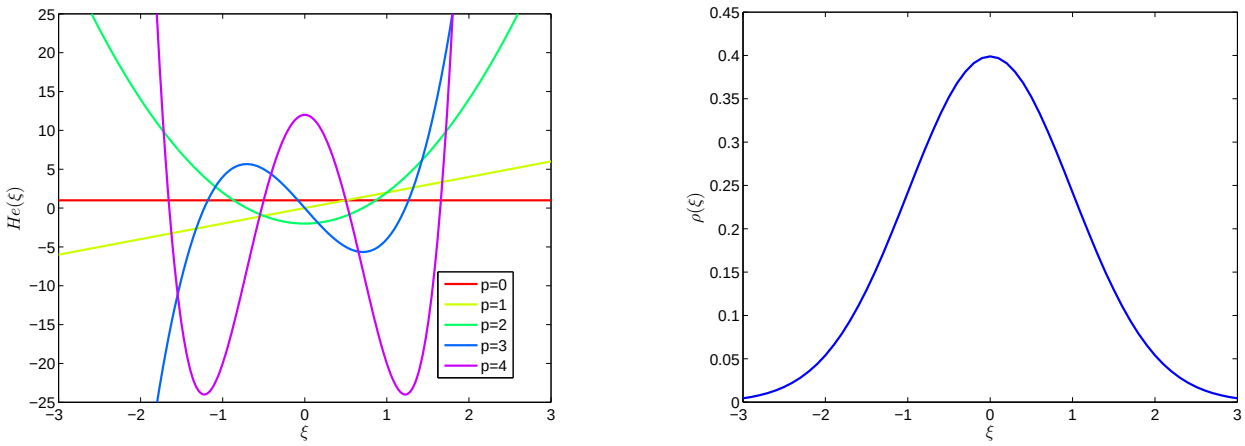

(a) (b)

Figure 1.1: (a) The first 5 Hermite polynomials and the (b) Gaussian Distribution.

QoI. The non-intrusive truncated system of equations can be explicitly written in matrix form as

$$\underbrace{\begin{bmatrix} \psi_1(\boldsymbol{\xi}^1) & \dots & \psi_P(\boldsymbol{\xi}^1) \\ \vdots & \vdots & \vdots \\ \psi_1(\boldsymbol{\xi}^N) & \dots & \psi_P(\boldsymbol{\xi}^N) \end{bmatrix}}_{\boldsymbol{\Psi}} \underbrace{\begin{bmatrix} c_1 \\ \vdots \\ c_P \end{bmatrix}}_{\boldsymbol{c}} = \underbrace{\begin{bmatrix} u(\boldsymbol{\xi}^1) \\ \vdots \\ u(\boldsymbol{\xi}^N) \end{bmatrix}}_{\boldsymbol{u}}$$

$$\boldsymbol{\Psi} \in \mathbb{R}^{N \times P}$$

$$\boldsymbol{c} \in \mathbb{R}^{P \times 1}$$

$$\boldsymbol{u} \in \mathbb{R}^{N \times 1}$$

where P represents the total expansion order of our polynomials and N corresponds to the number of samples of the QoI. The expansion coefficients can be identified via compressive sensing [9, 30, 51, 53], least squares regression [7, 81], or pseudo-spectral methods [84, 34, 25, 23], all of which represent non-trivial computational expenditures.

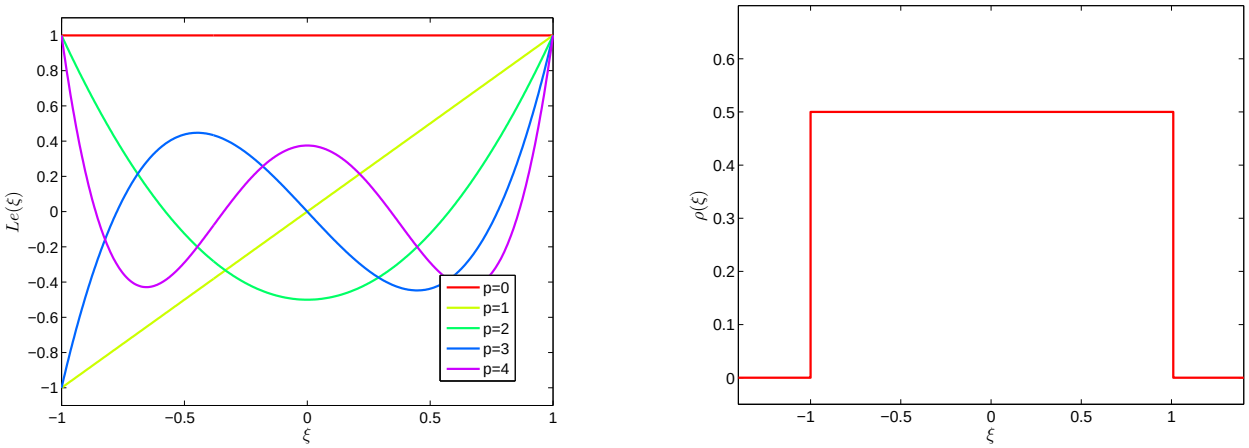

(a) (b)

Figure 1.2: (a) The first 5 Legendre polynomials and the (b) Uniform distribution.

1.4.1 Sampling methods - Least squares regression

The PCE system of equations may be solved via ℓ_2 minimization (also known as regression) by solving the following objective function:

$$\boldsymbol{c} = \{\arg\min_{\boldsymbol{c}} \|\boldsymbol{\Psi c} - \boldsymbol{u}\|_2\}. \tag{1.11}$$

In this expression $\|\cdot\|_2$ denotes the ℓ_2 norm. ℓ_2 minimization can be thought of as the regression of the exact solution $u(\boldsymbol{\xi})$ onto the PC basis. When $\boldsymbol{\Psi}$ is full rank, the solution to $\boldsymbol{c}$ can be found by solving the normal equation,

$$(\boldsymbol{\Psi}^T\boldsymbol{\Psi})\boldsymbol{c} = \boldsymbol{\Psi}^T\boldsymbol{u}. \tag{1.12}$$

A unique solution requires $N > P$ realizations of $u(\boldsymbol{\xi})$. It has been shown that for $d > p$ the required number of samples for a stable solution is

$$N \geq 3^p CP \log P \tag{1.13}$$

where C is an absolute constant [48]. N samples may be generated via Monte Carlo style sampling. Generating $N > P$ evaluations of the QoI may be impractical for complex problems, given that they are likely to be high dimensional, or require high total order approximations, or both. However, given sufficient smoothness of $u(\boldsymbol{\xi})$ with respect to $\boldsymbol{\xi}$, there is often some sparseness in the PC

basis, which results in many entries of $\boldsymbol{c}$ being zero (or nearly zero). Using methods borrowed from the field of compressive sampling, it is possible to exploit this "sparseness" and reconstruct $\boldsymbol{c}$ for $N < P$.

1.4.2 Sampling methods - Compressive sensing

Compressive sensing is an important aspect of signal processing concerned with the task of recovering sparse signals from limited or noisy data. The general idea is that, given an appropriate basis and a sparsity enforcing solver, many signals are sparse and can be reconstructed with very few samples [84]. Compressive sensing type methods have been used extensively in the fields of medical imaging and electrical engineering. In the context of PCE compressive sensing can be used to solve under-determined systems of equations, for $\boldsymbol{c}$. Consider the following system

$$\boldsymbol{\Psi c} = \boldsymbol{u} \tag{1.14}$$

where $\boldsymbol{\Psi}$, which is referred to here and in signal processing as the measurement matrix, is fat, (i.e. $N < P$). The PC system given in Equation (1.8) can be approximated by

$$\hat{u}(\boldsymbol{\xi}) = \sum_{j \in \mathcal{S}} c_j \psi_j(\boldsymbol{\xi}) \tag{1.15}$$

where $\mathcal{S}$ has fewer elements than P. The size of $\mathcal{S}$ is referred to as the "sparsity". Using combinatorial optimization techniques, compressive sensing seeks to solve the following problem:

$$P_0 = \{\arg\min_{\boldsymbol{c}} \|\boldsymbol{c}\|_0 \colon \boldsymbol{\Psi c} = \boldsymbol{u}\}, \tag{1.16}$$

wherein $\|\boldsymbol{c}\|_0$ is defined as the number of non-zero entries in c. In reality, this is an $N - P$ hard problem, and the cost of determining such a solution using ℓ_0 minimization can be prohibitively expensive. Subsequently, the ℓ_0 problem is often approximated by the ℓ_1 minimization problem

$$P_1 = \{\arg\min_{\boldsymbol{c}} \|\boldsymbol{c}\|_1 \colon \boldsymbol{\Psi c} = \boldsymbol{u}\}, \tag{1.17}$$

which can be solved using convex optimization solvers featuring linear programming. It has been shown that ℓ_1 optimization returns an optimal sparse solution as long as certain conditions, such

as the Restricted Isometry property (RIP) for the measurement matrix Ψ, are met [29, 28, 14]. For approximately sparse and noisy signals, it is more practical to solve the basis pursuit de-noising (BPDN) problem

$$P_{1,\epsilon} = \{\arg\min_{\boldsymbol{c}} \|\boldsymbol{c}\|_1 \colon \|\boldsymbol{\Psi c} - \boldsymbol{u}\|_2 \leq \epsilon\} \tag{1.18}$$

where the solution is relaxed by tolerance ϵ [20]. Here, ϵ designates the degree to which the observed data points $\boldsymbol{\xi}$ and $u(\boldsymbol{\xi})$ are fit, and care must be taken not to over-fit the data. Identification of an appropriate ϵ can be crucial to the accurate recovery of coefficients that fit not only $u(\boldsymbol{\xi})$ (u at sampled points) but the solution u at sample points yet to be seen. Ideally, $\epsilon \approx \|\boldsymbol{\Psi c}_{exact} - \boldsymbol{u}\|_2$, but as $\boldsymbol{c}_{exact}$ is unavailable, it can be estimated using cross-validation techniques. It was shown in [51] that for d dimensional Legendre polynomials of total order p, the number of samples required for a stable solution recovery is

$$N \geq 3^p CS \log P \tag{1.19}$$

where S is the number of dominant coefficients. Given that N in Equation (1.13) is linearly proportional to P and N in Equation (1.19) is proportional to S, it is evident that compressive sensing will require fewer samples than least squares for convergence, when $S < P$.

1.4.3 Sampling methods - Spectral Projection

Yet a third class of methods for estimating the PC coefficients are those that rely on integration rules. In so called pseudo-spectral methods the QoI is evaluated at abscissa which may be generated via a multi dimensional quadrature rule. A weighted interpolation strategy is then used between quadrature points to estimate the volume under the curve. In tensor product quadrature, abscissa are generated in d-dimensional space by the tensorization of 1-dimensional quadrature rules.

Solving for PCE coefficients with a quadrature rule is referred to as spectral projection (NISP for non-intrusive spectral projection). NISP solves for $\boldsymbol{c}$ by requiring that the error between the QoI and its approximation, $u(\boldsymbol{\xi}) - \sum_j c_j \psi_j(\boldsymbol{\xi})$, be orthogonal to the span of the polynomial basis,

i.e.,

$$\left\langle u(\boldsymbol{\xi}) - \sum_j c_j \psi_j(\boldsymbol{\xi}), \psi_j \right\rangle = 0 \tag{1.20}$$

which leads to

$$c_j = \langle u, \psi_j \rangle = \int_{\Xi} u(\boldsymbol{\xi}) \psi_j(\boldsymbol{\xi}) \rho(\boldsymbol{\xi}) d\boldsymbol{\xi}. \tag{1.21}$$

[84]. The integrals on the right hand side of Equation (1.21) are approximated using an N_q point quadrature rule where q refers to the number of quadrature points $1...N_q$, such as

$$c_j = \int_{\Xi} u(\boldsymbol{\xi}) \psi_j(\boldsymbol{\xi}) \rho(\boldsymbol{\xi}) d\boldsymbol{\xi} = \sum_{q=1}^{N_q} u(\boldsymbol{\xi}^q) \psi_j(\boldsymbol{\xi}^q) w^q. \tag{1.22}$$

Here, $\boldsymbol{\xi} = \{\boldsymbol{\xi}^1 ... \boldsymbol{\xi}^{N_q}\}$ is the set of quadrature points with corresponding weights w^q, which are tensorized versions of the 1-D weights. When utilizing Gaussian quadrature, Equation (1.22) exactly computes all polynomials less than degree $2N_q - 1$ [34]. The computational burden of determining coefficients in this fashion lies primarily in computing N_q model evaluations. In its most basic form, tensor product quadratures are isotropic in all directions, i.e., there are an equal number of tensorized grid points in each stochastic dimension d. Such schemes include Clenshaw-Curtis, which utilizes abscissa of Chebyshev polynomials, Gauss quadrature , or the most basic trapezoidal rule approximation. For low dimensional problems, tensorized quadrature rules can be exceedingly accurate (Gauss quadrature features polynomial accuracy of $2N^q - 1$, CC polynomial accuracy of $N^q - 1$) [56, 34]. Quadrature rules are highly susceptible to the curse of dimensionality however, as the most basic form scales like N_q^d. Sparse grid quadrature schemes, such as Smolyak sparse grids (first introduced by [79]), have been proposed to help reduce the number of required QoI evaluations. For the Smolyak sparse grid it can be shown that

$$N \approx 2^p \frac{d^p}{p!} \tag{1.23}$$

where $q = d + p$ is a level parameter dictating the sparsity [5, 63]. Also of interest are so-called adaptive sparse grids, [42] which adapt the number of quadrature points based on the complexity of the dimension. The Sparse Psuedospectral Approximation Method (SPAM) may offer further

improvement to sparse grids, which can exhibit unacceptable errors in predicting coefficients of higher order polynomials [23].

1.5 Motivation

All non-intrusive PCE methods are notably limited by the so-called "curse of dimensionality". This phrase, common to the worlds of UQ and optimization, is an allusion to the exponential dependence of the computational cost of performing iterative analysis on the dimension of the problem (see Eq. (1.7)). For highly accurate simulations, for which a single evaluation of the QoI may take minutes to days, sampling enough to form the PCE system of equations may represent a colossal expenditure. This has motivated the search for improvements to typical PCE techniques such as multi fidelity methods.

For a given application, the accuracy of a simulation is generally proportional to its computational cost. It is by this heuristic that one may define low and high fidelity models: namely, those that are less accurate but are correspondingly less expensive, and those that are more accurate, but are proportionally more expensive. Multi fidelity methods attempt to leverage the fast convergence of low fidelity models to help accelerate design/statistical iterations while sparingly sampling high fidelity models for corrective purposes. The resulting multi fidelity approximation of the QoI may achieve similar accuracy to a high fidelity model for computational cost of a low fidelity model. A comprehensive overview of the state of the art is given in [70]. In the niche realm of polynomial chaos, success has been demonstrated with additive/multiplicative corrections [64, 69], incorporation of gradient information [68], and other forms of correction functions [74, 33]. This thesis represents the contribution of two novel techniques to the growing field of multi fidelity PC.

1.5.1 Contributions of this thesis

The first method examined in this thesis is a weighted ℓ_1 minimization method which utilizes *a priori* information to promote sparsity in the PCE basis. The second method explored is a basis reduction method, which leverages a low fidelity model to form a spanning basis for a high fidelity

PCE. Numerical tests on physics based models for a lithium ion battery and an airfoil showcase the benefits and shortcomings of both techniques.

1.5.2 Bi fidelity weighted ℓ_1 minimization

Basic ℓ_1 minimization can be further improved with the introduction of a weighting matrix; this is known as weighted basis pursuit denoising method (WBPDN for short). The WBPDN objective function is the following:

$$P_{1,\epsilon}^{\boldsymbol{W}} = \{\arg\min_{\boldsymbol{c}} \|\boldsymbol{W}\boldsymbol{c}\|_1 \colon \|\boldsymbol{\Psi}\boldsymbol{c} - \boldsymbol{u}\|_2 \leq \epsilon\} \tag{1.24}$$

wherein the weighting scheme can sparsity in $\boldsymbol{c}$. Here, the coefficients of a low fidelity PCE are utilized to form $\boldsymbol{W}$. This method is based on the assumption that a while the exact values of the PCEs of a high fidelity model and a low fidelity model will differ, the sparsity and *relative* contributions of the basis terms will be similar.

1.5.3 Bi fidelity stochastic basis reduction

Using a Karhunen Loeve expansion one can form a spanning basis to the PC basis which may be significantly smaller in size. Unfortunately, to find such a reduced basis in this fashion still requires solving the PCE system of equations and may therefore be computationally infeasible for a high fidelity simulation. Making the assumption that errors between a low fidelity and high fidelity model in the stochastic dimension are independent of errors in the spatial/temporal dimension, a reduced basis is formed from the polynomial chaos expansion of a low fidelity model and used with limited high fidelity samples to form a bi-fidelity approximation. Significant improvements in accuracy over a high fidelity model alone are observed for all experiments.

With the preceding chapter we hope to have provided an overview of the current state of the art of polynomial chaos for UQ and motivated the need for multi fidelity PC techniques. The outline for the rest of this thesis as follows: Chapter 2 details the approach and numerical results of the weighted ℓ_1 method. Chapter 3 expounds upon the basis reduction method and offers numerical

results as proof of concept. Chapter 4 contains discussion, conclusions, and future work.

Chapter 2

Weighted L1 Minimization

2.1 Introduction

This chapter describes a new method for the recovery of sparse polynomial chaos expansions (PCEs) of high fidelity simulations via a weighted ℓ_1-minimization approach. Weighting is derived from *a priori* knowledge of the PC coefficients in the form of a low fidelity model. The weighted basis pursuit denoising algorithm (WBPDN) is then used with a limited number of high fidelity samples to yield a bi fidelity approximation of the PC coefficients. Proof of concept is demonstrated upon two airfoil simulations subject to six stochastic dimensions (one at high Mach number, one at low), and one lithium ion battery (LIB) simulation subject to 17 stochastic dimensions. Response prediction accuracies are compared for weighted ℓ_1 minimization against both low and high fidelity solutions using an equivalent numbers of high fidelity samples.

2.2 Compressive Sensing

Compressive sensing is a class of methods concerned with the low-complexity recovery of signals admitting S sparse representations given a small number of signal samples, i.e. $N < P$. As an alternative to regression, truncated PCE is approximated by

$$\hat{u}(\boldsymbol{\xi}) = \sum_{j \in C} c_j \psi_j(\boldsymbol{\xi}) \tag{2.1}$$

where C has fewer elements than P, assuming a certain level of sparsity in $\boldsymbol{c}$. Using combinatorial optimization techniques, compressive sensing solves for $\boldsymbol{c}$ via the following minimization problem:

$$P_0 = \{\arg\min_{\boldsymbol{c}} \|\boldsymbol{c}\|_0 \colon \boldsymbol{\Psi c} = \boldsymbol{u}\} \tag{2.2}$$

wherein $\|\boldsymbol{c}\|_0$ is defined as the number of non-zero entries in $\boldsymbol{c}$. Solving the ℓ_0 minimization system is an $N-P$ hard problem [13] (the computational equivalent of a sudoku puzzle), and is commonly approximated by the ℓ_1 minimization problem

$$P_1 = \{\arg\min_{\boldsymbol{c}} \|\boldsymbol{c}\|_1 \colon \boldsymbol{\Psi c} = \boldsymbol{u}\}, \tag{2.3}$$

which has a computationally tractable solution. Equation (2.3) is solved using optimization methods based on linear programming techniques and is an $O(N^3)$ hard problem [16] (a much more feasible task than solving Equation (2.2)). In seminal works by [15, 16] it has been shown that ℓ_1 minimization returns a comparable solution to ℓ_0 as long as the signal is sufficiently sparse and $\boldsymbol{\Psi}$ satisfies the Restricted Isometry property (RIP) [39]. For a given measurement matrix $\boldsymbol{\Psi} \in \mathbb{R}^{N\times P}$ the $\delta_S = \delta_S(\boldsymbol{\Psi})^{\text{th}}$ RIP parameter of $\boldsymbol{\Psi}$ is defined as the smallest quantity $\delta \in (0,1)$ that satisfies

$$(1-\delta)\|\boldsymbol{c}\|_2^2 \leq \|\boldsymbol{\Psi c}\|_2^2 \leq (1+\delta)\|\boldsymbol{c}\|_2^2 \tag{2.4}$$

for all S-sparse vectors $\boldsymbol{c} \in \mathbb{R}^{1\times P}$. In essence, the RIP requires that all sparse vectors in $\boldsymbol{\Psi}$ form an approximately orthonormal basis [89]. Several theorems exist to describe the relationship between the RIP and the likelihood of exact recovery of S-sparse signals via ℓ_1 minimization. For further information the reader is referred to [39].

Each ℓ_p space (ℓ_2, ℓ_1, and ℓ_0, etc.) can be geometrically visualized as a volume [50] in d dimensional space, as in Fig. 2.2. Norm minimization algorithms effectively contract or expand the contour of the ℓ_p space until reaching a solution that satisfies a given system of equations. The choice of norm influences the set of possible solutions - which may or may not include the sparsest $\boldsymbol{c}$. As p decreases, the corresponding ℓ_p volume decreases, thereby reducing the potential contact points with a given solution. Smaller values of p help to promote sparsity; in the instance of the ℓ_0 ball the only possible solutions lie on one of the axes. However, ℓ_p norm minimization for $p < 1$

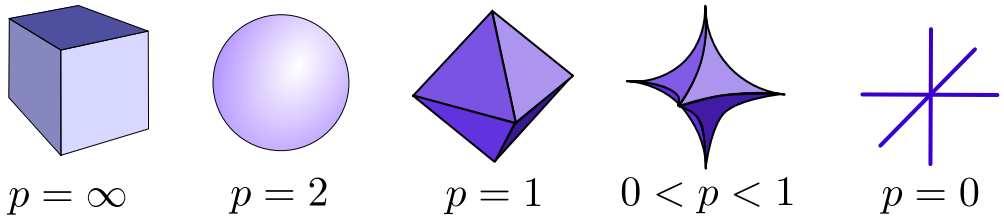

Figure 2.1: A comparison of the different ℓ_p norms of $\boldsymbol{c}$ in three dimensions.

is strongly $N - P$ hard [40]. As such the ℓ_1 or ℓ_2 norms are generally looked to for solving large systems of equations. One possible recourse to this dilemma is to weight the ℓ_1 norm. Weighting the ℓ_1 norm allows us to further influence the set of possible solutions while still employing time-tested ℓ_1 minimization algorithms.

2.3 Weighted BPDN

In reality, many signals are noisy or may be only approximately sparse. For these types of problems it is more appropriate to solve the Basis Pursuit De-Noising (BPDN) problem:

$$P_{1,\epsilon} = \{\arg\min_{\boldsymbol{c}} \|\boldsymbol{c}\|_1 \colon \|\boldsymbol{\Psi c} - \boldsymbol{u}\|_2 \leq \epsilon\}. \tag{2.5}$$

The minimization of $\|\boldsymbol{c}\|_1$ promotes sparsity in $\boldsymbol{c}$ by reducing the number of non-zero entries, while at the same time satisfying the relationship $\boldsymbol{u} = \boldsymbol{\Psi c}$ by $\|\boldsymbol{\Psi c} - \boldsymbol{u}\|_2 \leq \epsilon$ within a prescribed tolerance. The tolerance, ϵ, designates the degree to which the observed data points $\boldsymbol{\xi}$ and $u(\boldsymbol{\xi})$ are fit, and care must be taken not to over-fit the data. Identification of an appropriate ϵ can be critical in accurately recovering $\boldsymbol{c}$.

Typical BPDN algorithms tend to punish larger terms in $\boldsymbol{c}$ more heavily than smaller terms in order to minimize the $\|\boldsymbol{c}\|_1$ term. This can hinder the recovery of an optimally sparse signal as more small coefficients may be retained than necessary. It has been shown that the introduction of a weighting matrix to the BPDN problem can further enhance sparsity by deforming the ℓ_1 ball. An illuminating description of this deformation for a generic signal can be found in [35] and it is adapted here for the PCE problem in Fig. 2.2. The weighted BPDN objective function is the

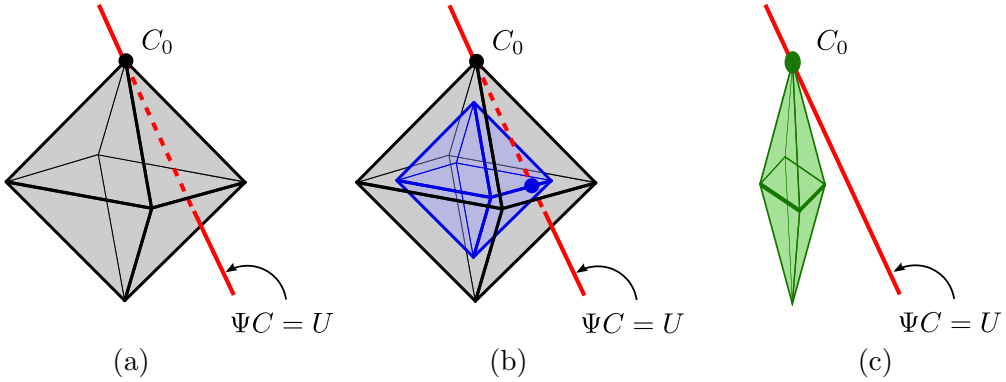

Figure 2.2: Recovery of a sparse $\boldsymbol{c}_0$ via standard and weighted ℓ_1 minimization. (a) The signal, $\boldsymbol{c}_0 \in \mathbb{R}^3$ has a sparsity of 1 (i.e., has one non-zero entry) and therefor exists as a point on one of the axes of the ℓ_1 ball. Assuming our system is under-determined, ($\boldsymbol{u}$ contains two or fewer measurements) $\boldsymbol{\Psi}$ has a nullity of 1 (represented by the red line). Any point along this line satisfies $\boldsymbol{\Psi C} = \boldsymbol{U}$. It can be seen in (b) that there exists $\boldsymbol{c} \neq \boldsymbol{c_0}$ for which $\|\boldsymbol{c}\|_1 < \|\boldsymbol{c_0}\|_1$, resulting in the algorithm returning a non-sparse $\boldsymbol{c}$. Weighting the ℓ_1 term, as in (c), reduces the size of the solution space, enforcing $\boldsymbol{c} \neq \boldsymbol{c_0}$ for all $\|\boldsymbol{Wc}\|_1 < \|\boldsymbol{Wc_0}\|_1$, and thereby increasing the likelihood of returning a sparse $\boldsymbol{c}$.

following:

$$P_{1,\epsilon}^{\boldsymbol{W}} = \{\arg\min_{\boldsymbol{c}} \|\boldsymbol{Wc}\|_1 \colon \|\boldsymbol{\Psi c} - \boldsymbol{u}\|_2 \leq \epsilon\}, \tag{2.6}$$

where $\boldsymbol{W}$ is a diagonal weighting matrix. A number of schemes for constructing the $\boldsymbol{W}$ have been suggested in the literature, but fundamentally, $\boldsymbol{W}$ is intended to steer the algorithm towards one solution or another. Subsequently, the weights must be selected with great care, either using theoretical analysis, or *a priori* information. Selecting the weights to be inversely proportional to the expected signal entries, as in

$$w_j = (c_j)^{-1}, \tag{2.7}$$

enforces a more "democratic" punishment of the entries of $\boldsymbol{c}$, as large entries are effectively decreased, and smaller entries effectively increased.

Various formulations for $\boldsymbol{W}$ have been proposed including iterative re-weighting ([35, 19, 88]). Unfortunately, such schemes can be prohbitively expensive, as they require iterative sampling of the ℓ_1 solving algorithm. Some success has also been shown using theoretical guarantees on the decay of coefficients [52]. Such methods tend to be very problem specific however. The remainder

of Chapter 2 is devoted to the exploration of the use of *a priori* information about the decay of the coefficients using a low fidelity PCE, known as the multi fidelity WBPDN.

2.4 Multi fidelity WBPDN

In the multi fidelity WBPDN, the entries of the weighting matrix, $\boldsymbol{W}$, are given by

$$w_j = (c_j^L + \delta)^{-1} \tag{2.8}$$

where c_j^L is the j^{th} PC coefficient of a low fidelity model. Forming the weighting matrix in this way forces the recovered signal to have a similar sparsity to $\boldsymbol{c}^L$. The locations of non zero entries are retained, at the same relative magnitudes, but the exact values of the PC coefficients will not be the same in $\boldsymbol{c}^H$ and $\boldsymbol{c}^L$. The introduction of δ serves two purposes: 1) it ensures that there is no division by zero, and 2) it sets a limit for the smallest coefficient that will be retained. If δ is set to be a fraction of the largest low fidelity coefficient,

$$\delta = \delta_w \max(\boldsymbol{c}^L) \tag{2.9}$$

than all coefficients less than this are excluded. Studies have shown that the WBPDN method is somewhat robust to the choice of δ_w [35] and it was set to $1e-3$ for all studies after a simple cross validation study (detailed in Appendix A). Doing so effectively precludes all coefficients smaller than $1e-3 \times \max(\boldsymbol{c}^L)$ from the resulting solution. The bi fidelity system of equations is then formed with limited numbers of high fidelity samples and solved via the multi fidelity WBPDN objective function as

$$P_{1,\epsilon}^{\boldsymbol{W}} = \{\arg\min_{\boldsymbol{c}} \|\boldsymbol{W}\boldsymbol{c}\|_1 \colon \|\boldsymbol{\Psi}^H\boldsymbol{c} - \boldsymbol{u}^H\|_2 \leq \epsilon\}. \tag{2.10}$$

Here, $\Psi^H \in \mathbb{R}^{N^H \times P}$ is the measurement matrix evaluated at N^H high fidelity samples and $\boldsymbol{u}^H \in \mathbb{R}^{N^H \times 1}$. The Spectral Projected Gradient algorithm SPGL1 package for MATLAB® was employed to solve all BPDN/WBPDN problems. The tolerance on the ℓ_2 residual was set to $\epsilon = 1e-3 \times norm(\boldsymbol{u})$ for all tests.

2.5 Test Problems

Three benchmark problems were used to explore the multi fidelity WBPDN method. The first and second studies concern NACA0012 airfoils, one at low Mach number, one at a higher range. Both were subject to uncertainties in Mach number, angle of attack, and geometry. The third study concerns a lithium ion battery (LIB) simulation, subject to 17 uncertain parameters.

2.6 NACA0012 airfoil

The NACA airfoil series is a family of airfoils whose geometry is dictated via analytical equations that describe the thickness and curvature of the geocentric centerline. The NACA 4 digit series are defined by 4 parameters: maximum camber m in percentage of the total airfoil chord length, the maximum camber p as a percentage of the chord length, and maximum thickness t as a percentage of the chord length. Airfoil performance is primarily measured through C_D, the drag coefficient and C_L, the lift coefficient. Both of these forces results from the pressure distribution over the surface of an airfoil [72], a quantity which is captured by the pressure coefficient C_f. For low speed flow, C_f can be written as

$$C_f = \frac{P - P_\infty}{1/2\rho U^2} \tag{2.11}$$

where P is static pressure, P_∞ is the free stream pressure, U is free stream velocity and ρ is fluid density.

2.6.1 Mach number M

Mach number is a dimensionless variable that inversely relates the flow velocity U past an object to the speed of sound,c as:

$$M = \frac{U}{c}. \tag{2.12}$$

Mach number is primarily used to determine the degree to which a flow can be treated as incompressible. For $M < 1$, subsonic flow, compressibility can be ignored. At $M = 1$ a flow is said be

transonic, and compressibility effects become very important. At $M > 1$ a flow is said to be supersonic (or hypersonic above $M > 3$) and compressible conditions and shock waves are generated by the object. Two ranges of M were tested - high and low M. In both cases M was treated as a uniformly distributed random variable.

2.6.2 Angle of attack α

The angle of attack refers to the angle between the chord of an airfoil and the direction of the surrounding flow of fluid around it. The lift coefficient of an airfoil is a direct function of α, and therefore is very closely related to boundary layer separation, which may be unpredictable and difficult to simulate accurately. Here, α is treated as uniformly distributed.

2.6.3 Geometrical Parameters

Several geometrical parameters are also incorporated in the stochastic model. Camber is a measure of the asymmetry between the top and bottom surfaces of an airfoil. Effectively, it gives the thickness above the meridian line that divides the top and bottom surfaces. Adding camber (asymmetry) to an airfoil generally increases the lift coefficient. Maximum camber (m) is given by

$$\frac{m}{c} \times 100 = \%camber, \tag{2.13}$$

and is here used as a uniformly distributed random variable. Chord length c, which refers to the distance between the leading edge and trailing edge of an airfoil, is used as a random variable, as is the location of maximum camber as a fraction of chord length, p, and the maximum thickness as a fraction of chord length t. t is given by

$$\frac{t}{c} \times 100 = \%thickness. \tag{2.14}$$

These parameters can be seen in Fig. 2.3. A summary of the different inputs and their distributions is given in 2.6.3. Given that all inputs are uniformly distributed, tensorized Legendre polynomials of each variable were used in forming the PCE.

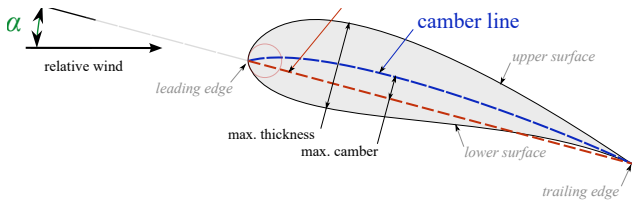

Figure 2.3: NACA0012 airfoil parameters.

2.7 Numerical Tests

High and low fidelity commercial CFD codes were used to simulate the pressure coefficient, C_p, over the surface of a NACA0012 airfoil as function of the 6 random variables. The low fidelity model used was XFOIL [32], a coupled inviscid/viscous solver. It features rudimentary transition and turbulence models, boundary layer equations, and is generally known to be accurate only in the subsonic regime of flow. A given analysis took < 1 second. The high fidelity model used was FLUENT®, a finite volume CFD code, which uses the Spallart-Almaras turbulence model and a NASA mesh with boundary layer resolution. In contrast to XFOIL, a given analysis could take several minutes. The pressure profile was measured at 128 grid points along the surface of the airfoil for 1200 total ensembles of random inputs for both high and low fidelity studies. This study was conducted for two different Mach number ranges, one at relatively low Mach number and one at relatively high Mach. These shall be referred to as airfoil Tests 1 and 2 respectively.

The performance of the multi fidelity WBPDN method was contrasted to a reference solution, a low fidelity solution, and a high fidelity solution with a limited number of samples. The low fidelity PCE approximation of the QoI, u^L, was generated using the regular BPDN method with all available low fidelity samples ($N^L = 1200$). A high fidelity model, u^H, was also generated with the regular BPDN using a number of high fidelity samples, N^H, which is considered insufficient to return an accurate solution. Also computed was a reference PCE, which was formed using all available high fidelity samples, denoted as u^{Ref}. In these studies u^{Ref} is held as the gold standard for accuracy among the available models. It is used only for comparison purposes, so as to demonstrate the

Random Input	Nominal Value	Distribution
high M	0.2	Uniform, [0.1, 0.3]
low M	0.4	Uniform, [0.3, 0.4]
α	0°	Uniform, [-3, 3]
m	0.2	Uniform, [0, 0.4]
c	1.125	Uniform, [0.75, 1.5]
p	0.4	Uniform, [0.3, 0.5]
t	0.125	Uniform, [0.1, 0.15]

Table 2.1: List of random airfoil inputs used in this study.

efficacy of each method. The multi fidelity WBPDN method was then used to generate a bi fidelity approximation, u^B. Given that the computational cost for a low fidelity sample N^L is negligible compared to that for high fidelity sample, all metrics are given as a function of N^H. The total expansion order in each case was $p = 5$, resulting in 462 basis terms per expansion ($\mathbf{\Psi} \in \mathbb{R}^{N\times 462}$). The mean can easily be generated from the PCE as:

$$\mu_u = c_1. \tag{2.15}$$

The variance can be generated from:

$$\sigma_u^2 = \sum_{j=2}^{P} c_j^2. \tag{2.16}$$

Samples of the mean C_p profile are shown in Fig. 2.4 and Fig. 2.5 for the low and high M airfoil problems, respectively. The two bundles of curves in each plot represent a superposition of the pressure coefficient on the upper and lower surfaces of the airfoil; this is common practice for showcasing C_p. Each bundle contains 4 lines: the reference mean, the high fidelity mean for low N^H, the low fidelity mean and the bi fidelity mean. Black denotes the reference solution, which is the PC approximation of the high fidelity model using all available high fidelity samples ($N^{Ref} = 1200$). Green corresponds to the low fidelity approximation, u^L. Red represents the high fidelity PC approximation formed using low N^H samples. Blue represents the bi fidelity solution, which uses high and low fidelity samples ($N^H = 10$ and $N^L = 1200$). Upon closer inspection it can be seen that the low fidelity model (green) in Fig. 2.4 better predicts the reference solution than Fig. 2.5. This makes sense given that the low fidelity model would struggle to capture the

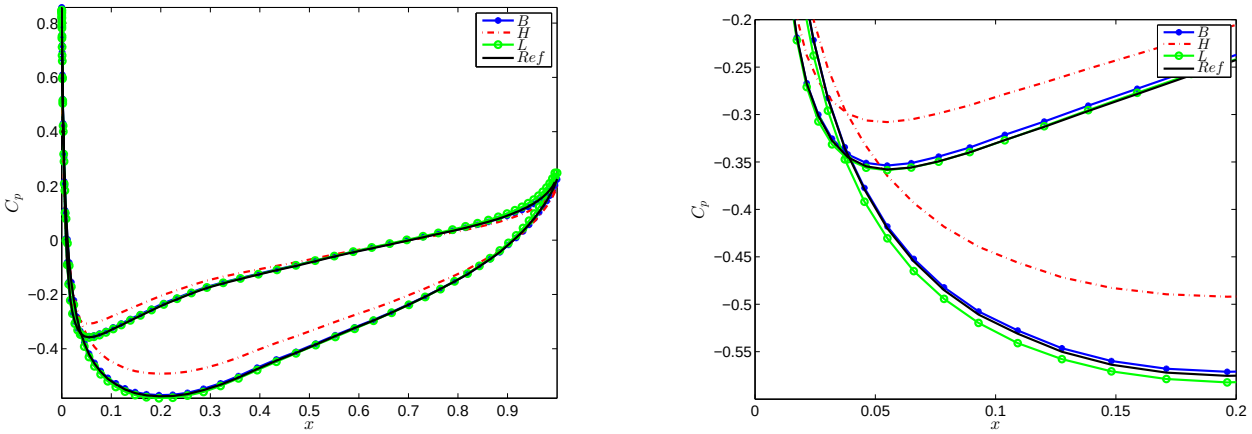

(a) (b)

Figure 2.4: (a) A sample mean profile for $N^H = 10$ for airfoil Test 1 alongside (b) a close up of mean for airfoil Test 1.

nuances of C_p as M increases. This trend is also observable in Fig. 2.6 and in Fig. 2.7 which show sample profiles of the variance of C_p for the low and high M tests respectively. The high fidelity model, which features very low N^H, seems to give the poorest approximation of the reference solution. The mean and variance profiles shown in Fig. 2.4, Fig. 2.5, Fig. 2.6 and Fig. 2.7 were generated using 100 ensembles of $N^H = 10$ and averaged. The discrepancy between models was then quantified using the following metrics.

2.7.1 Metrics

The quality of approximation was characterized by two metrics, namely, the normalized ℓ_2 error of the mean with respect to the reference mean

$$err_\mu = \frac{\|\boldsymbol{\mu}^{Ref} - \boldsymbol{\mu}\|_2}{\|\boldsymbol{\mu}^{Ref}\|_2} \tag{2.17}$$

and the normalized ℓ_2 error of the variance with respect to the reference variance

$$err_{\sigma^2} = \frac{\|\boldsymbol{\sigma}^{Ref^2} - \boldsymbol{\sigma}^2\|_2}{\|\boldsymbol{\sigma}^{Ref^2}\|_2}. \tag{2.18}$$

The mean and variance as given in Equations (2.17) and (2.18) were generated for 100 ensembles of N^H samples and averaged. This was done for a range of N^H.

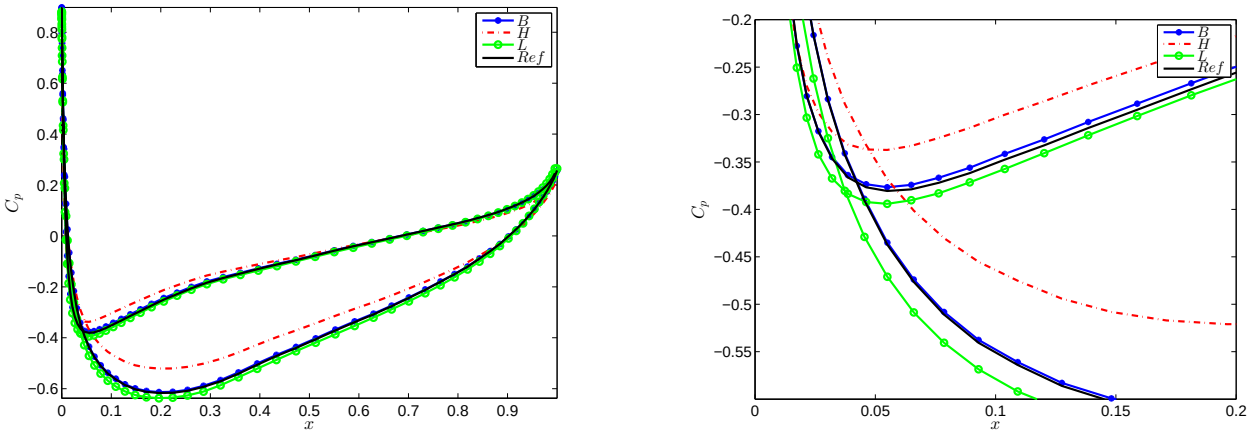

(a) (b)

Figure 2.5: (a) A sample mean profile for $N^H = 10$ alongside (b) a close up of the mean for airfoil Test 2.

2.7.2 Results

The average relative errors in the mean for airfoil Test 1 and 2 as a function of $N^H = 10 : 110$ can be seen in Fig. 2.8 and Fig. 2.9, respectively. Evaluations of the low fidelity model are computationally trivial compared to the high fidelity model, so all quantities are plotted as a function of N^H.It can be seen in both cases that the high fidelity model performs poorly in predicting the mean initially but overtakes the bi fidelity method around $N^H = 60$. In both cases, the variance in the mean error is consistently lower for the WBPDN method than the high fidelity model. The bi fidelity error plateaus around $N^H = 60$.

The relative errors in variance as a function of $N^H = 10 : 110$ for airfoil Tests 1 and 2 can be seen in Fig. 2.10 and Fig. 2.11. Again, it can be observed that the average relative error in variance of the low fidelity model is lower for the low M range, indicating that higher M is problematic for the low fidelity solver. The average error in variance is consistently lower for the entire range of samples than the high fidelity model. Though it is not explicitly observed here, it is expected and inevitable that the high fidelity model will eventually converge to the bi fidelity approximation in accuracy.

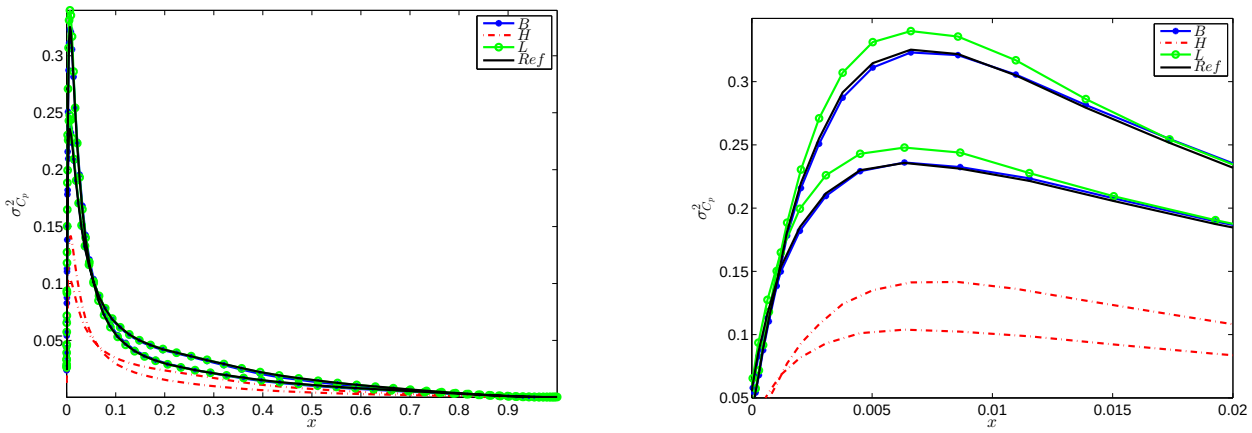

(a) (b)

Figure 2.6: (a) A sample variance profile for $N^H = 10$ alongside (b) a close up of the variance for airfoil Test 1.

2.8 Lithium Ion Battery Model

The next example under consideration is a stochastic, physics based model for a Lithium-Ion Battery (LIB). LIBs are popular for both consumer and commercial purposes as they are known for their high energy density, good temperature range, low memory effect and long battery life. In the particular battery model considered here, the anode is made from Lithium-Cobalt oxide $LiCoO_2$. The 2 main components of a LIB are the electrolyte and the electrodes. During discharge, oxidation occurs at the anode and yields electrons to an external circuit, while the LiC_6 cathode is reduced by accepting the electrons back. Separating the two electrodes is an electrolyte. When the battery is being charged Li^+ ions migrate from the anode to the graphite layers of the cathode. A schematic of a LI battery is shown in Fig. 2.12.

The fundamental metric for characterizing remaining battery life of a LIB is the distribution of Li ions between anode and cathode, referred to as the liquid ion concentration, $\mathcal{C}$. The discharge cycle of a $LiC_6/LiCoO_2$ cell was simulated as a function of 17 uncertain input parameters, listed in Fig. 2.8.7, at a discharge rate of $4C$. The primary QoI studied was the liquid phase concentration at a time snapshot of $t = 2000s$. Samples of the mean and variance of $\mathcal{C}$ for reference, high, low, and bi fidelity methods, as described in the previous section, can be seen in Fig. 2.13.

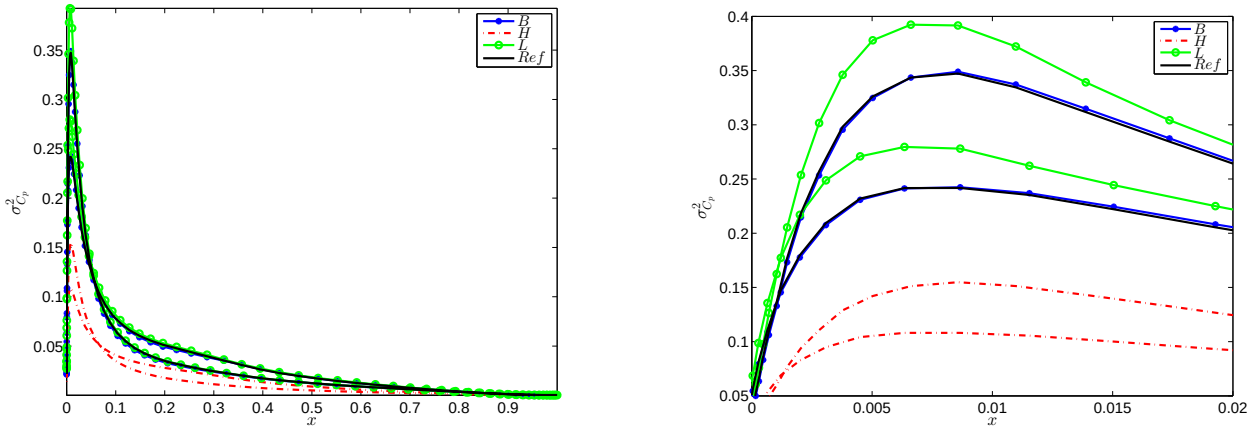

(a) (b)

Figure 2.7: (a) A sample variance profile for $N^H = 10$ alongside (b) a close up of the variance for airfoil Test 2.

All model parameter ranges given are unique to the $LiC_6/LiCoO_2$ cell. Due to limited data in the literature regarding the distributions of the parameters some assumptions had to be made about their form. $\mathcal{C}$ was simulated using Newman's model on a fine and coarse mesh, which are considered the high and low fidelity models, respectively. The interested reader is directed to [47] for a detailed description of the simulation, as well as a discussion of contemporary methods for incorporating uncertainty into LIB simulations. The following section details the stochastic parameters used. Exact numerical values can be found in table 2.8.7.

2.8.1 Porosity ϵ

Porosity is the fraction of the volume of the pores to the total volume in the battery. There tends to be an inverse relationship between porosity and capacity [78]. Based on experimental data, uniform distributions are assumed for the porosity at the anode, cathode, and separator.

2.8.2 Bruggeman coefficient, brugg

A volume averaged formulation is often used in porous electrode theory to describe the position and shapes of pores and particles, as opposed to specifying them exactly [82]. For the anode, cathode, and separator, uniform distributions were selected.

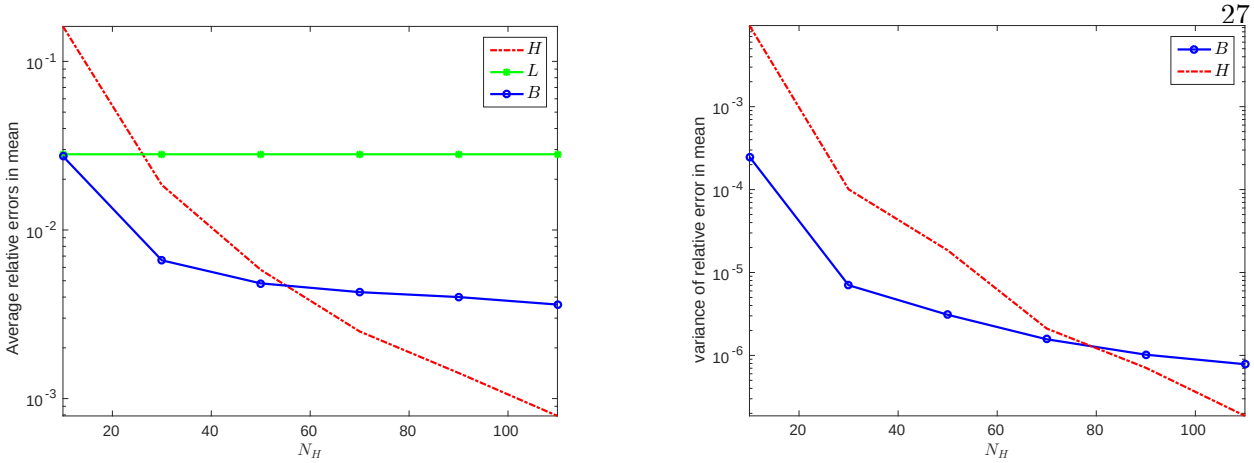

(a) (b)

Figure 2.8: (a) The average of the normalized error of the mean of err_μ and (b) the variance of err_μ for airfoil Test 1.

2.8.3 LI^+ transference number, t_+^0

The transference number defines the portion of current carried by the LI^+ ions during discharge of the battery. The transference t_+^0 is positively correlated with battery power. A uniform distribution was assumed.

2.8.4 Diffusion coefficients, D and D_s

The salt diffusion coefficient in the liquid phase, D, characterizes the friction forces between the ions and the solvents [66]. It is critical to have a high D to restrict salt concentration gradients, which impede performance. Salt diffusion coefficient is positively correlated to battery power. We assume it to have a uniform distribution. Also considered is the Diffusion coefficient of the solid, D_s for all three battery sections. D_s impacts the performance of LIBs by impacting the intercalation flux. For the anode, cathode, and separator, uniform distributions were selected.

2.8.5 Electronic conductivities, σ and σ_s

The capacity of LIBS is partially a function of the solid phase electronic conductivity σ_s [21]. There is limited available data about the distribution of σ_s, as it is often treated as a constant

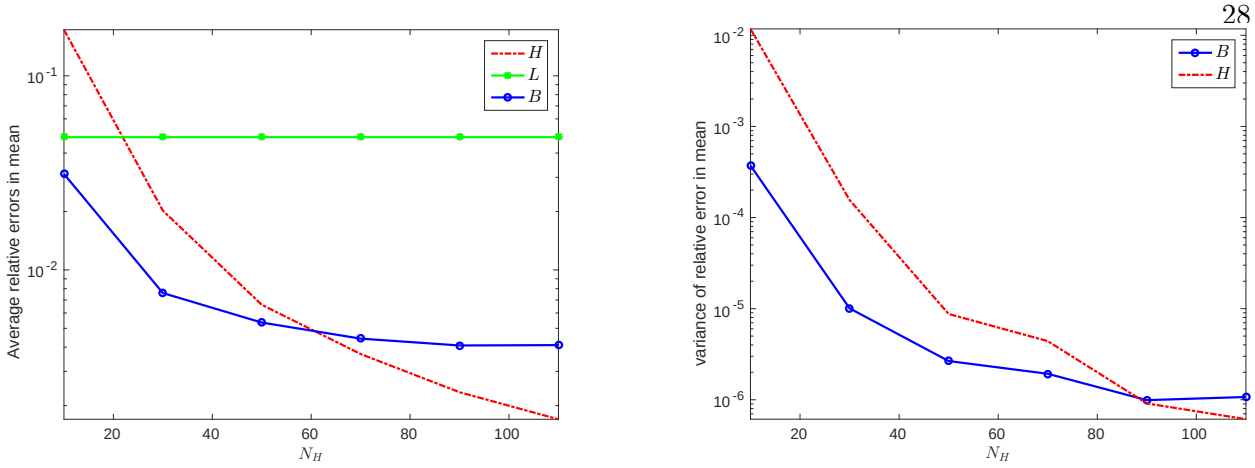

Figure 2.9: (a) The average of the normalized error of the mean of err_μ and (b) the variance of err_μ for airfoil Test 2.

in the literature. We assume it to be normal distributed. The conductivity of the electrode material is given by σ. There is a positive correlation between the battery capacity and the solid phase electronic conductivity [47]. Both the anode and cathode were selected to be uniformly distributed.

2.8.6 Reaction rate constant k

The reaction rate constant k can be calculated by known the initial state of the battery [71]. There is a positive correlation between reaction rate constant and reversibility of the battery cycle. We assume its distribution to be uniform for anode, cathode, and separator.

2.8.7 Additional parameters

Also examined were some geometrical uncertainties, such as the lengths of the electrodes and separator. All parameters and their distributions are summarized in Table 2.8.7. Note that all parameters featured uniform distributions so Legendre polynomials were used in their PCE's. A total expansion order of P=3 was used resulting in 1140 basis terms in the expansion.

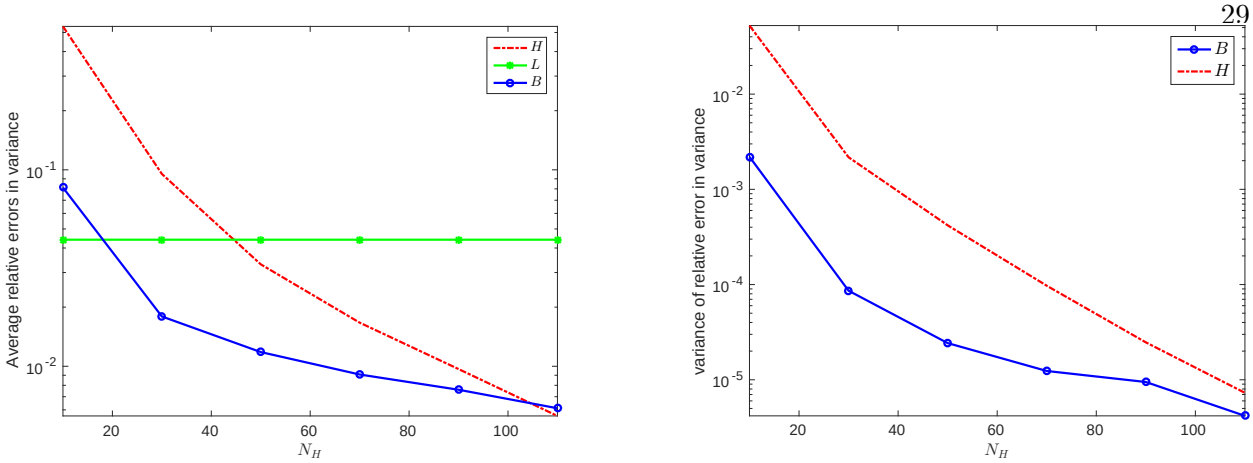

(a) (b)

Figure 2.10: (a) The average of the normalized error of the variance of err_{σ^2} and (b) the variance of err_{σ^2} for airfoil Test 1.

Random Input	Nominal Value	Distribution
ϵ_a	0.485	Uniform, [0.46, 0.51]
ϵ_s	0.724	Uniform, [0.63, 0.81]
ϵ_c	0.385	Uniform, [0.36, 0.41]
brugg_a	4	Uniform, [3.8, 4.2]
brugg_s	4	Uniform, [3.2, 4.8]
brugg_c	4	Uniform, [3.8, 4.2]
t_+^0	0.363	Uniform, [0.345, 0.381]
D $[\text{m}^2 \cdot \text{s}^{-1}]$	7.5×10^{-10}	Uniform, [6.75, 8.25] $\times 10^{-10}$
$D_{s,a}$ $[\text{m}^2 \cdot \text{s}^{-1}]$	3.9×10^{-14}	Uniform, [3.51, 4.29] $\times 10^{-14}$
$D_{s,c}$ $[\text{m}^2 \cdot \text{s}^{-1}]$	1×10^{-14}	Uniform, [0.9, 1.1] $\times 10^{-14}$
σ_a $[\text{S} \cdot \text{m}^{-1}]$	100	Uniform, [90, 110]
σ_c $[\text{S} \cdot \text{m}^{-1}]$	100	Uniform, [90, 110]
k_a $[\text{m}^4 \cdot \text{mol} \cdot \text{s}]$	5.03×10^{-11}	Uniform, [4.52, 5.53] $\times 10^{-11}$
k_c $[\text{m}^4 \cdot \text{mol} \cdot \text{s}]$	2.334×10^{-11}	Uniform, [2.10, 2.56] $\times 10^{-11}$
L_a $[\mu\text{m}]$	80	Uniform, [77, 83]
L_s $[\mu\text{m}]$	25	Uniform, [22, 28]
L_c $[\mu\text{m}]$	88	Uniform, [85, 91]

Table 2.2: List of random LIB inputs used in this study.

2.9 Numerical tests

PC approximations of $\mathcal{C}$ were generated using the high fidelity model (for limited N^H), low fidelity model, reference model and bi fidelity model. Using Equation (2.17), the average of the relative error in mean as a function of N^H can be seen in Fig. 2.14 alongside the variance

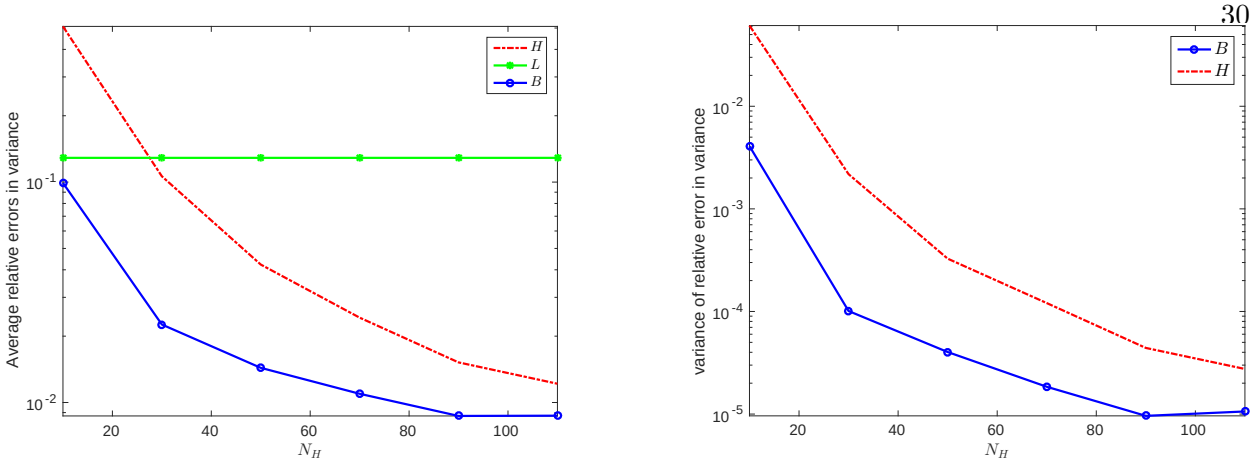

(a) (b)

Figure 2.11: (a) The average of the normalized error of the variance of err_{σ^2}, and (b) the variance of err_{σ^2} for airfoil Test 2.

of the same quantity. The average of the relative error in variance, given in Equation (2.18), along with the variance of this quantity can be seen 2.15. Just as in the airfoil examples, the multi fidelity WBPDN method outperforms the high fidelity model for low N^H in predicting the reference solution. By $N^H = 60$ however, the high fidelity model outperforms the bi fidelity method in predicting the mean. However, the bi fidelity method continues to outperform the high fidelity model in predicting the variance until $N^H = 180$.

2.10 Discussion

It was observed in all test cases that the multi fidelity WBPDN method outperforms the low fidelity model and the high fidelity model in predicting the reference mean and variance. It also tends to do so with less variance than the high fidelity model. The bi fidelity method obviously shines in predicting the variance above the mean. In all three test cases the high fidelity model tends to outperform the bi fidelity model around $N^H = 60$ in predicting the mean, yet the bi fidelity prediction of the variance continues to outperform well past that point in all cases. This could be due to the fact that the bi fidelity model reproduces the overall contributions of the coefficients without being particularly accurate with respect to any single coefficient. Subsequently, the mean,

which is calculated from the first coefficient in the expansion, might be more obviously impacted by these discrepancies. The variance however, which is calculated as

$$\sigma_u^2 = \sum_{i=1}^{r} c_i^2 \tag{2.19}$$

and resembles a norm itself, may be more robust to small discrepancies among coefficients.

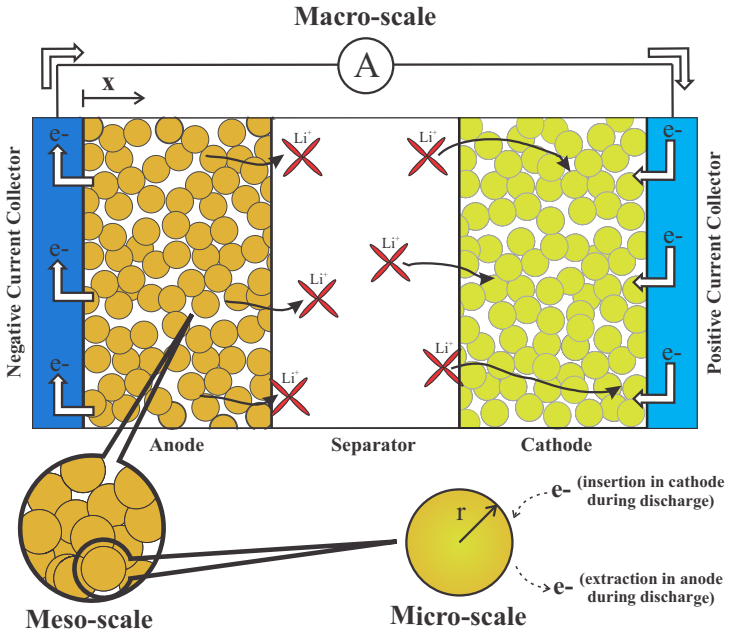

Figure 2.12: LIB schematic. Image taken courtesy of [47].

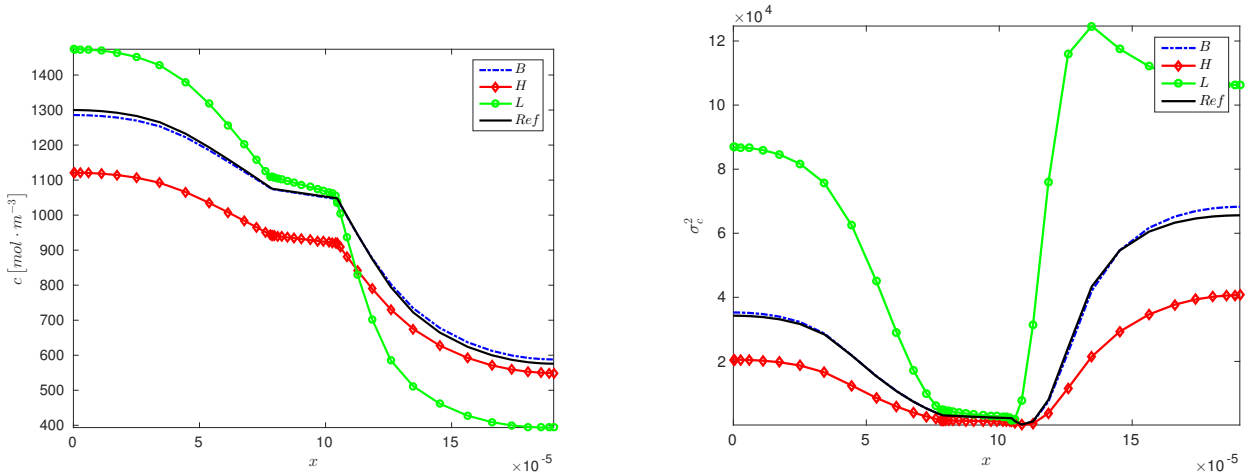

(a) (b)

Figure 2.13: (a) A sample of the mean and (b) variance profiles as predicted by u^H ($N_H = 30$), u^L, u^{Bi}, and u^{Ref} for the LIB model.

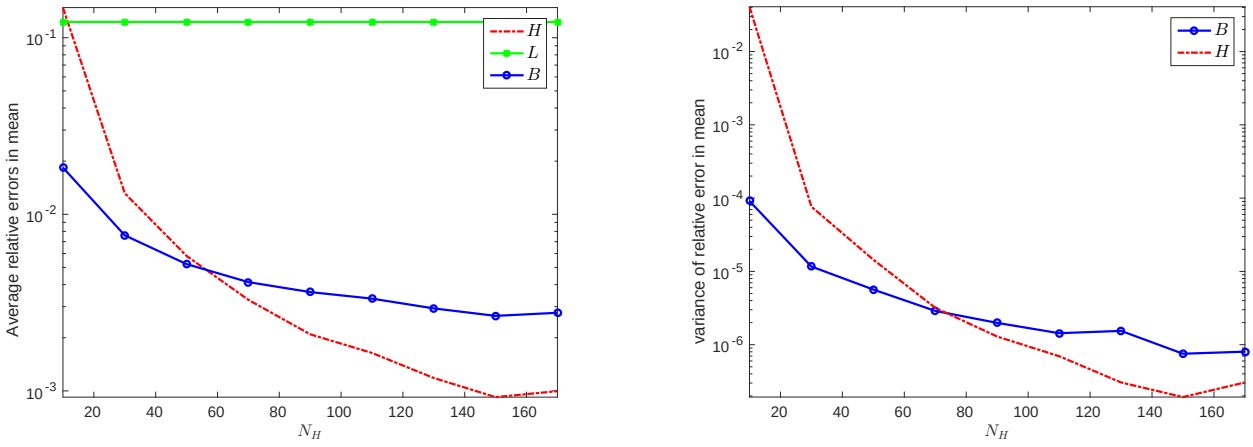

(a) (b)

Figure 2.14: (a) The average of the mean error and (b) the variance of the mean error for LIB model.

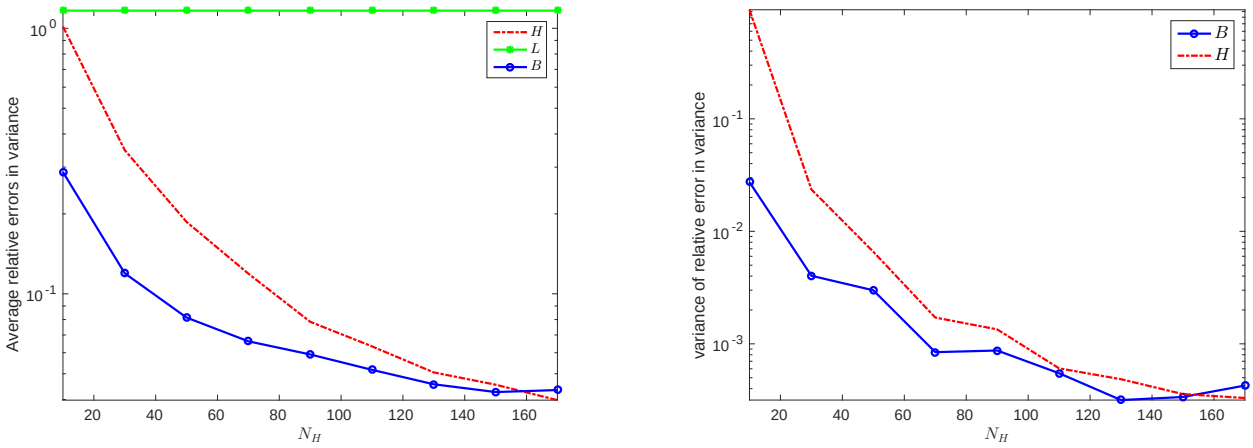

(a) (b)

Figure 2.15: (a) The average of the variance error and (b) the variance of the variance error for LIB model.

Chapter 3

Stochastic Reduced Basis Method

3.1 Introduction

This chapter explores a bi fidelity method for approximating a high fidelity quantity of interest (QoI) with a low-dimensional manifold of polynomial chaos (PC) basis functions. The low-dimensional manifold is identified using principle component analysis (PCA) of the nodal covariance of a low fidelity model. This method relies on the assumption that errors in the stochastic space are independent of physics-based errors and therefore a good approximation of the covariance can be obtained using a low fidelity model. Analysis of the benchmark problems introduced in Chapter 2 indicate greater returns in accuracy over a high fidelity PCE for an equivalent number of samples.

3.2 Model Reduction

The objective of Reduced Order Modeling (ROM) is to obtain a parsimonious description of multivariate data. Principal Component Analysis (PCA) is a classical dimension reduction technique that transforms a set of observations of correlated variables into an orthogonal basis of linear uncorrelated variables. PCA can be thought of as revealing the internal structure of data in a way that best captures the variance of the data [54]. PCA appears under such monikers as Proper Orthogonal Decomposition (POD) and is closely related Singular Value Decomposition (SVD). The PCA basis is identified via eigenvalue decomposition of the nodal covariance matrix of the QoI. It has been shown in multiple studies that considering only a few basis functions can result

in a ROM that accurately approximates the QoI. PCA based model reduction has been applied with much success to fluids problems, [75, 11], which tend to be high dimensional in nature and require model reduction to eliminate degrees of freedom. Closely related to PCA is the Karhunen Loeve expansion (KLE), a form of spectral decomposition for stochastic processes. The KLE uses principle component analysis to form a reduced uncorrelated basis from the nodal covariance of the solution field of the QoI. The KLE provides an optimal representation of $u(x)$ in that, for a given M-term expansion truncation, the mean squared error of the approximation is minimized as compared to any other potential basis. It is leveraged here to form a reduced basis which spans the PCE basis and will ultimately require fewer evaluations of a potentially expensive QoI to solve. The mathematical formulation of the KLE follows.

3.3 Karhunen - Loeve Expansion

To form the KLE, eigenvalue decomposition is performed on the nodal covariance of the solution field of the QoI. Consider the following spectral representation of the QoI vector, $\boldsymbol{u} = u(x)$:

$$u(x, \boldsymbol{\xi}) = \langle u(x) \rangle + \sum_{i=1}^{\infty} (u(\cdot, \boldsymbol{\xi}) - \langle u(x) \rangle \, \phi_i(x)), \phi_i(x). \tag{3.1}$$

Here, $\{\phi_i(x)\}$ is an orthonormal basis with inner product defined by $\langle \cdot, \cdot \rangle$. The spatial variable is given by $x \in \mathbb{R}^{K \times 1}$. Because $(u(\cdot, \boldsymbol{\xi}) - \langle u(x) \rangle \, , \phi_i(x))$ is a random variable, it permits the following representation:

$$(u(x, \boldsymbol{\xi}) - \langle u(x) \rangle \, , \phi_i(x)) = \sqrt{\lambda_i} \eta_i(\boldsymbol{\xi}), \tag{3.2}$$

where η_i is a zero mean random variable with unit variance and $\sqrt{\lambda_i}$ is a normalizing constant. This basis and normalizing constant are found from the covariance matrix of $u(x, \boldsymbol{\xi})$, R. Because R is positive semi-definite it can be restructured in terms of a sequence of positive eigenvalues λ_i with corresponding eigenfunctions $\phi_i(x)$. $\phi_i(x)$ and λ_i are revealed by eigenvalue decomposition of

$$R\phi_i(x) = \lambda_i \phi_i(x). \tag{3.3}$$

The covariance R of $u(x, \boldsymbol{\xi})$ can easily be estimated from a polynomial chaos expansion as:

$$R(x_1, x_2) = \sum_{j=2}^{P} c_j(x_1) c_j(x_2), \tag{3.4}$$

where c_j are the PCE coefficients.

The eigenvalues and eigenvectors in Equation (3.3) are then used as basis functions

$$u(x, \boldsymbol{\xi}) = \langle u(x) \rangle + \sum_{i=1}^{\infty} (u(x, \boldsymbol{\xi}) - \langle u(x) \rangle, \phi_i(x)), \tag{3.5}$$

which yields

$$u(x, \boldsymbol{\xi}) = \langle u(x) \rangle + \sum_{i=1}^{\infty} \sqrt{\lambda_i} \eta_i(\boldsymbol{\xi}) \phi_i(x). \tag{3.6}$$

The expansion in 3.6 is known as the KLE. For most practical applications, the solution field is discrete. Subsequently, the KLE is a finite expansion of at most K terms, the size of the solution field x. The magnitude of the eigenvalues (λ_k) are indicative of the relative contributions to the variance along principle orthogonal axes. Based on the ordinarily rapid decay of λ_k the KLE is truncated to r terms. One heuristic for truncation is

$$\alpha = \frac{\sum_{k=1}^{r} \lambda_k}{\sum_{k=1}^{K} \lambda_k}, \tag{3.7}$$

where α represents the percentage of eigenvalue data captured by an r term truncation, out of the total available eigenvalues K.

The formation of the KLE requires the covariance of the solution $u(x, \boldsymbol{\xi})$. Generating the solution space of a high fidelity QoI may be prohibitively expensive. If, however, it is assumed that errors in the stochastic space are independent of physics-based errors (discretization, modeling assumptions, etc.), the KL random variables can be estimated from a low fidelity solution $\boldsymbol{u}^L$, [2]. Once this is performed, the new basis is rewritten as a linear combination of PCE functionals.

3.4 Projection onto the PCE basis

The optimal basis set η_i can be rewritten as a linear combination of PC polynomials by equating the KL expression of $u(x)$ with its PC expression

$$\sum_{j=1}^{P} c_j^L(x) \psi_j(\boldsymbol{\xi}) = \langle u(x) \rangle + \sum_{i=1}^{r} \sqrt{\lambda_i} \eta_i(\boldsymbol{\xi}) \phi_i(x). \tag{3.8}$$

Subtracting the mean from both sides of (3.8) yields

$$\sum_{j=2}^{P} c_j^L(x)\psi_j(\boldsymbol{\xi}) = \sum_{i=1}^{r} \sqrt{\lambda_i}\phi_i(x)\eta_i(\boldsymbol{\xi}). \tag{3.9}$$

The new basis, η_i, is solved for from

$$\eta_i(\boldsymbol{\xi}) = \sum_{j=2}^{P} \frac{\left\langle \phi_i(x), c_j^L(x) \right\rangle}{\sqrt{\lambda_i}} \psi_j(\boldsymbol{\xi}). \tag{3.10}$$

is effectively a linear transformation of the PCE basis with r terms. When λ_i decays quickly $r \ll P$. The bi fidelity system can be constructed with the new reduced basis as

$$u^H(x,\boldsymbol{\xi}) \approx u^B(x,\boldsymbol{\xi}) = \sum_{i=1}^{r} c_i^B(x)\eta_i(\boldsymbol{\xi}) \tag{3.11}$$

where the bi fidelity coefficients, c_i^B, are solved for via regression. In matrix form Equation (3.11) can be written as

$$\underbrace{\begin{bmatrix} 1 & \eta_1(\boldsymbol{\xi}^1) & \dots & \eta_r(\boldsymbol{\xi}^1) \\ \vdots & \vdots & \vdots & \\ 1 & \eta_1(\boldsymbol{\xi}^{N^H}) & \dots & \eta_r(\boldsymbol{\xi}^{N^H}) \end{bmatrix}}_{\boldsymbol{\Psi}^B} \underbrace{\begin{bmatrix} c^1(x) \\ \vdots \\ c^{r+1}(x) \end{bmatrix}}_{\boldsymbol{c}} = \underbrace{\begin{bmatrix} u(x,\boldsymbol{\xi}^1) \\ \vdots \\ u(x,\boldsymbol{\xi}^{N^H}) \end{bmatrix}}_{\boldsymbol{u}^H}$$

$$\boldsymbol{\Psi}^B \in \mathbb{R}^{N^H \times r+1}$$

$$\boldsymbol{c} \in \mathbb{R}^{r+1 \times 1}$$

$$\boldsymbol{u}^H \in \mathbb{R}^{N^H \times 1}.$$

Given that $r \ll P$, this system of equations requires far fewer evaluations N^H of the high fidelity QoI, $\boldsymbol{u}^H$, to solve.

Proof of concept was first demonstrated in [2] (2007) when the basis reduction method was performed on an intrusive PCE system of equations. More recently, a reduced basis orthogonal non-intrusive PCE method was used for fluids problems with stochastic geometry [26]. In this study the low and high fidelity models were mesh refinements of the same solver. The method examined here is similar to [26]; however, here we show the viability of the method when the high

and low fidelity models are *two distinct* solvers (XFOIL and FLUENT®). A lithium ion battery (LIB) model is also studied, wherein the low and high fidelity models are different meshes of the same solver.

3.5 Numerical Tests

The basis reduction method was applied to two airfoil simulations (one at low M, one at high) and a lithium ion battery (LIB) simulation. The quantity of interest for the airfoil problems is the pressure coefficient C_p along the surface of the foil. For the LIB study, the quantity of interest was the liquid concentration $\mathcal{C}$ across the battery at a snapshot of $t = 2000s$. The basis reduction method was used to generate a PC approximation to the high fidelity model, which shall be denoted by $\boldsymbol{u}^B$. Also computed was a high fidelity PCE which will be referred to as $\boldsymbol{u}^H$, which is under-sampled. A low fidelity PCE, formed using all available low fidelity samples will be referred to as $\boldsymbol{u}^L$. A reference PCE, generated by extensively sampling the high fidelity model, is denoted as $\boldsymbol{u}^{Ref}$, and it is the gold standard against which all other models are compared. The mean of the reference, low and high fidelity models at a given point can be estimated from the PC expansion as

$$\langle u \rangle = c_1. \tag{3.12}$$

The variance σ can be calculated from

$$\sigma_u^2 = \sum_{j=2}^{P} c_j^2. \tag{3.13}$$

The mean and variance of the bi fidelity model are similarly calculated to be:

$$\langle u \rangle = c_1 \tag{3.14}$$

and

$$\sigma_u^2 = \sum_{i=1}^{r} c_i^2. \tag{3.15}$$

The two main metrics used to evaluate performance for these methods are the mean and

variance of normalized error between a given method and a reference solution as given by

$$err_{\mu} = \frac{\|\boldsymbol{\mu}^{Ref} - \boldsymbol{\mu}\|_2}{\|\boldsymbol{\mu}^{Ref}\|_2} \tag{3.16}$$

and

$$err_{\sigma^2} = \frac{\|\boldsymbol{\sigma}^{Ref^2} - \boldsymbol{\sigma}^2\|_2}{\|\boldsymbol{\sigma}^{Ref^2}\|_2} \tag{3.17}$$

respectively. The variance of both quantities given in Equation (3.16) and Equation (3.17) was also analyzed. Mean and variance here refer to ensemble mean and variance, as each experiment was repeated 100 times for a given number of high fidelity samples, N^H.

Also examined was the truncation rank of the approximation. Table 3.5 shows α, which is calculated from Equation (3.7) and represents the percentage of eigenvalue data captured by an r term truncation, out of the total available eigenvalues. Any $r > 10$ for both airfoil simulations and for the LIB simulation was found to result in $\alpha = 1$.

r	1	2	3	4	5	6	7	8
AF Test 1	86.44%	93.40%	98.76%	99.49%	99.82%	99.92%	99.98%	99.99%
AF Test 2	86.20%	93%	98.60%	99.42%	99.77%	99.88%	99.98%	99.99%
LIB	96.31%	98.72%	99.35%	99.75%	99.87%	99.94%	99.97%	99.99%

Table 3.1: Table of relative error in eigenvalue data as a function of rank r.

3.5.1 Airfoil Results

The average relative errors in the mean as a function of $N^H = 20 : 120$ and rank $r = 1, 3, 8, 12$ for airfoil Tests 1 and 2 can be seen in Fig. 3.1 and Fig. 3.2. Fig. 3.3 and Fig. 3.4 shows statistics of the variance. It is evident that increasing the rank of approximation causes an improvement in approximation of the bi fidelity model; however, a plateau is observed and around $err_{\mu} \approx 1e-3$ for the mean for both tests, and a plateau for $err_{\sigma^2} \approx 1e-2.5$. Airfoil Test 1 performs slightly better, as might be expected given that the low fidelity model better approximates the reference model for low M. Over the range of N^H selected, the high fidelity model never offers an improvement over $r = 8$ or $r = 12$, either in predicting the variance, or the mean, or in the variances of the errors

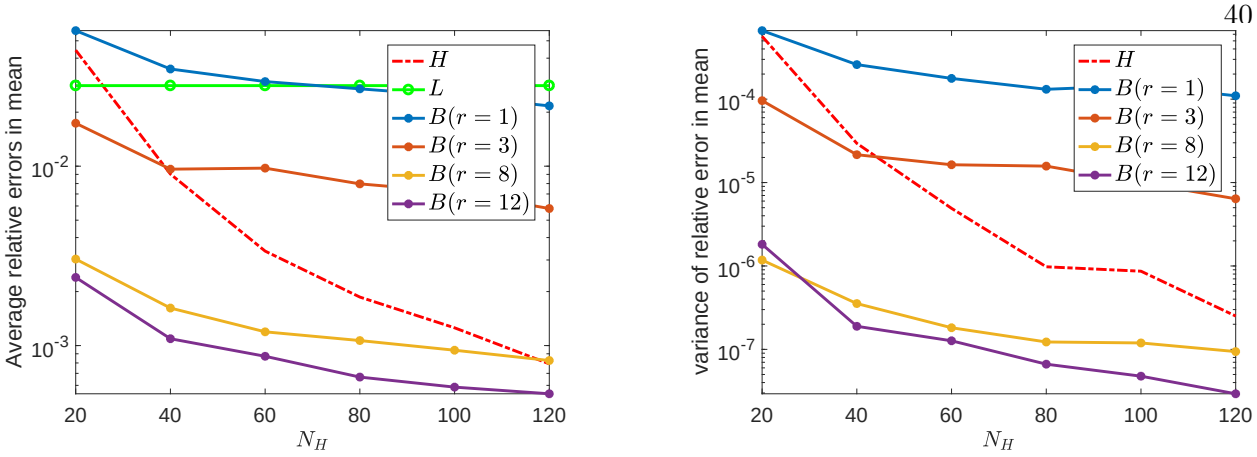

Figure 3.1: (a) The average of the error of the mean and (b) the variance of the error of the mean for airfoil Test 1.

of these quantities for airfoil Test 1. For airfoil Test 2, the high fidelity model only improves upon these quantities at the very end of our range of N^H.

3.5.2 LIB Results

The statistics of the mean and variance of $\mathcal{C}$ for the LIB can be seen in Fig. 3.5 and Fig. 3.6. As with both airfoil problems, it is evident that the rank 8 and rank 12 approximations offer improvement over the high fidelity model for most of N^H in predicting the mean. What is somewhat surprising is that the rank 8 approximation actually outperforms slightly the rank 12 approximation in predicting the variance. This is indicative that there may be an optimal rank of approximation, above which errors are reintroduced. An examination of the eigenvalues of the covariance matrix may help to shed light on this phenomena.

3.6 Discussion

The efficacy of the basis reduction method can be partially understood by examining the decay of the eigenvalues of the covariance matrices (low, high, and reference models). The more similar the decay of the eigenvalues of the low fidelity model to the eigenvalues of the reference model, the more accurate the bi fidelity approximation will be. As was seen in both airfoil problems,

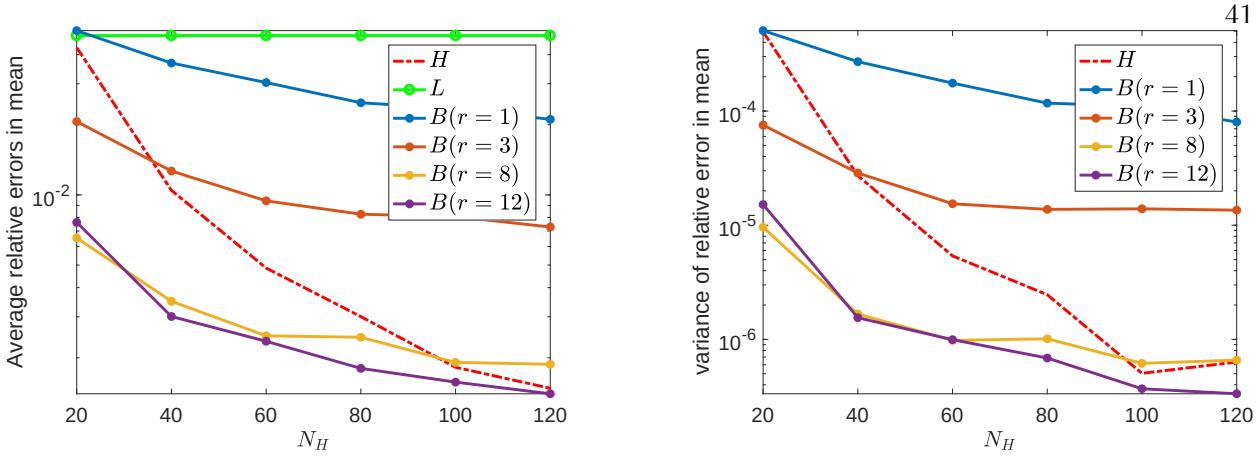

Figure 3.2: (a) the average of the error of the mean (b) the variance of the mean error for airfoil Test 2.

the rank 8 and 12 approximations consistently outperformed the high fidelity model, with the rank 12 performing best. Fig. 3.7 shows the first 8 eigenvalues of the airfoil models for the reference model, the high fidelity model and the low fidelity model for $N^H = 10$. It can be seen that the low fidelity model does a much better job in predicting the eigenvalues of the covariance of the reference model than the high fidelity model. For the LIB simulation however (eigenvalues shown in Fig. 3.8), the low fidelity model captures well the first few eigenvalues, but by the 5th eigenvalue no longer obviously outperforms the high fidelity model. As the variance is calculated using (3.15) the addition of more nodes will impact the accuracy of the variance, but not necessarily the accuracy of the mean, which is based only on the first coefficient. It seems likely that there is an optimal range of r, above which there is a reintroduction of low fidelity modeling errors. As this is likely problem specific, optimal r may be non-trivial to determine.

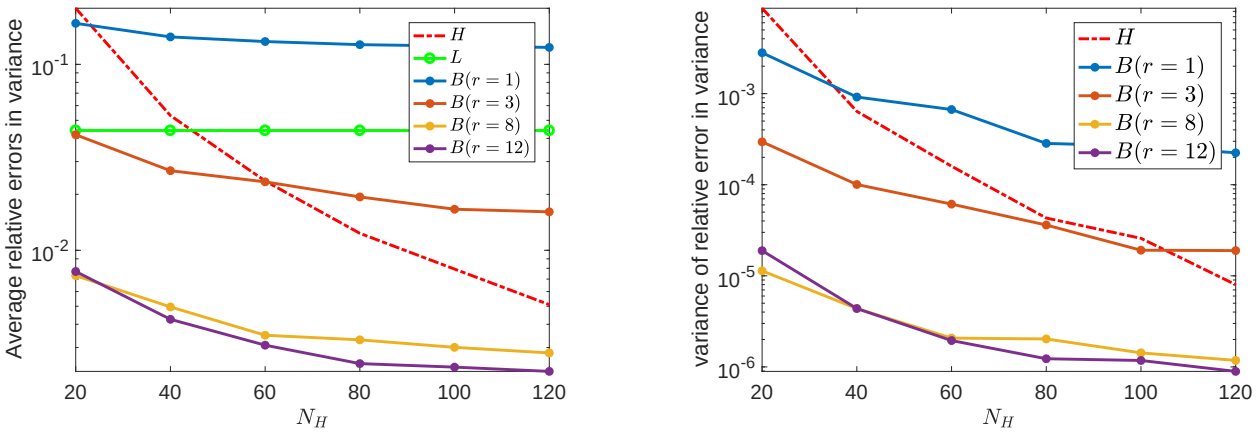

(a) (b)

Figure 3.3: (a) The mean variance and (b) the variance of the variance for airfoil Test 1.

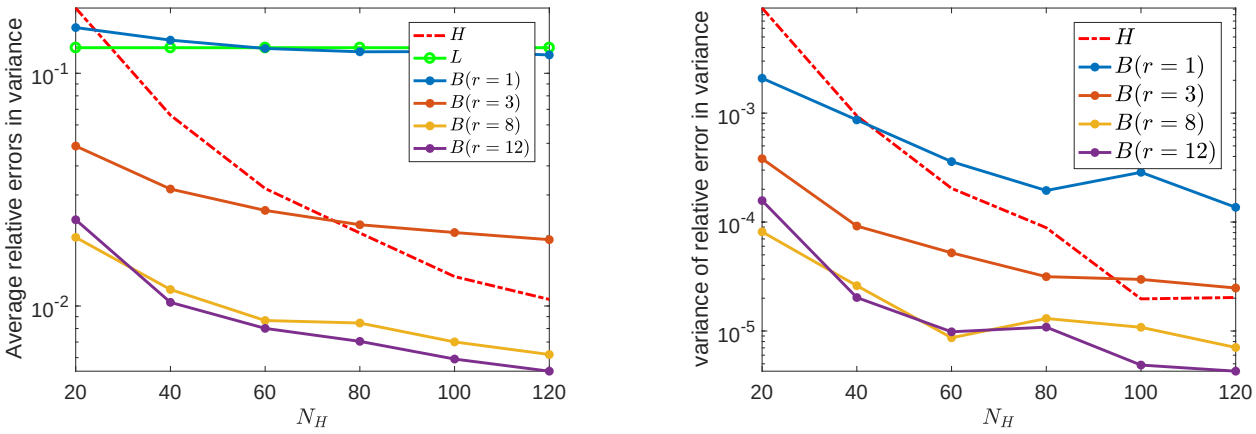

(a) (b)

Figure 3.4: (a) The average of the error of the variance and (b) the variance of the variance for airfoil Test 2.

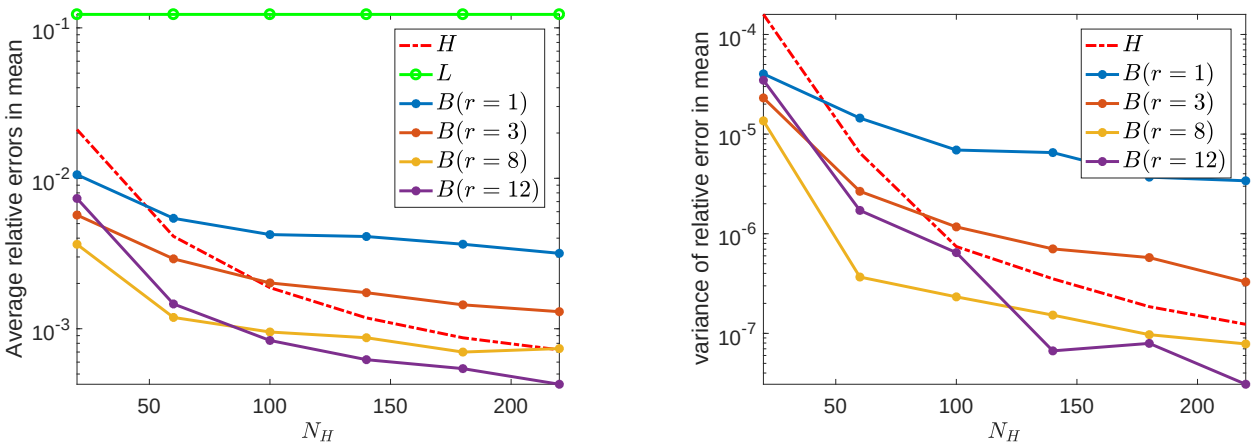

Figure 3.5: (a) The average error of the mean and (b) the variation of the error of the mean for LIB model.

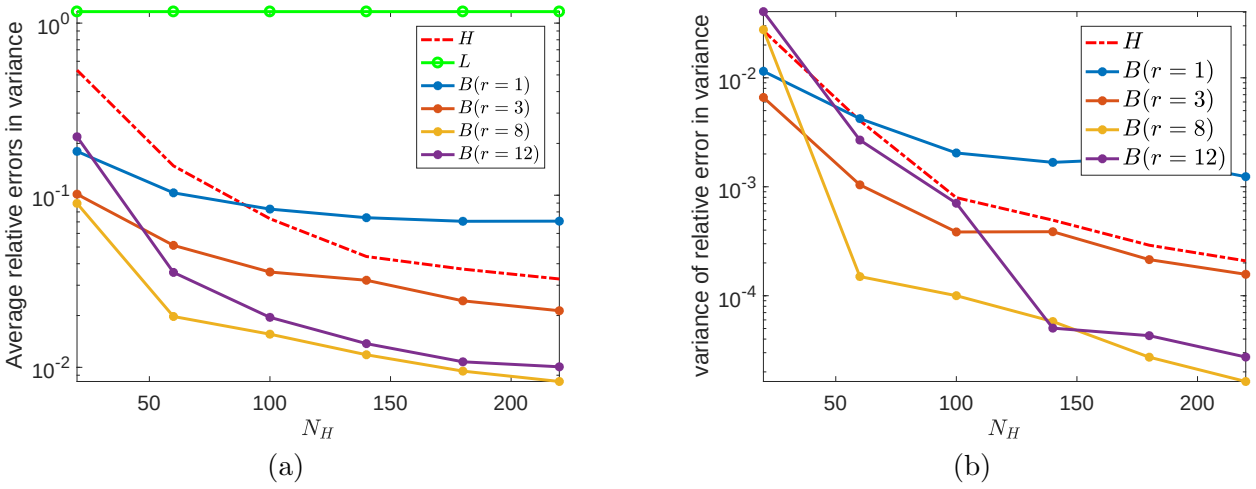

Figure 3.6: (a) The average error of the variance and (b) the variance of the error in predicted variance for LIB model.

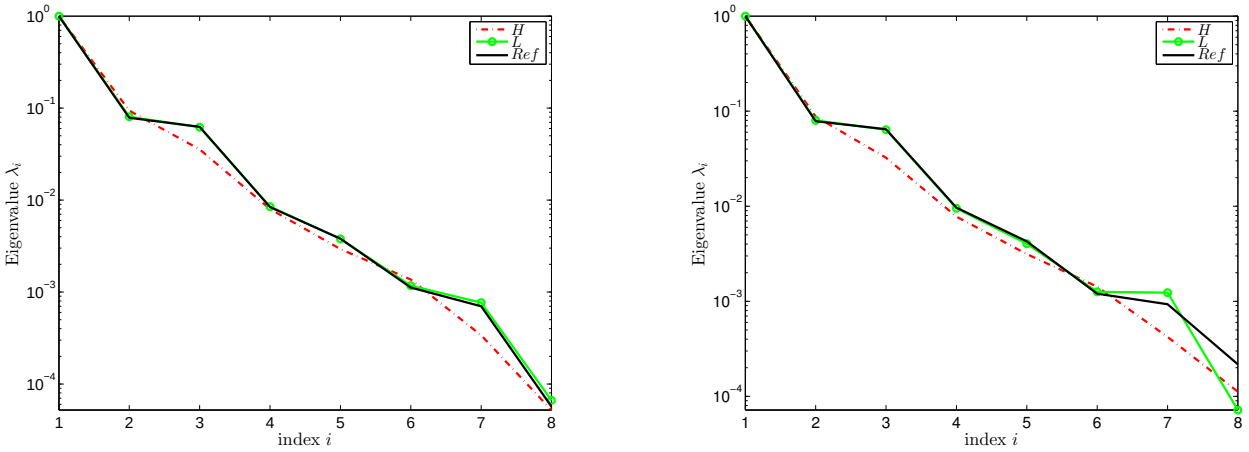

Figure 3.7: (a) Normalized eigenvalues for airfoil Test 1 (b) and airfoil Test 2.

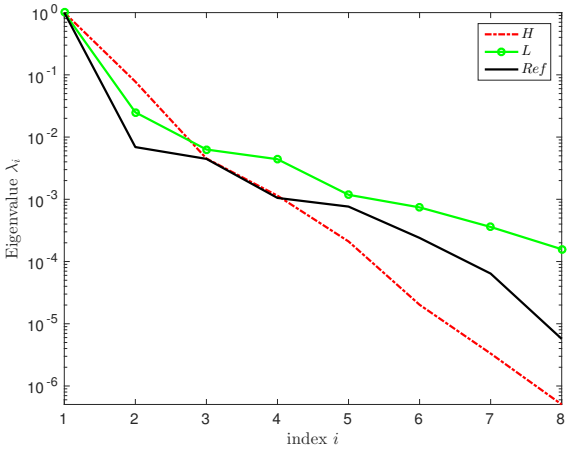

Figure 3.8: Normalized Eigenvalues of the LIB model for $N^H = 30$.

Chapter 4

Conclusion

4.1 Summary

This thesis presented two multi fidelity techniques for efficiently generating PC representations of high fidelity quantities of interest. A weighted ℓ_1 minimization method was employed to promote sparsity in the PCE of a high fidelity model, thereby decreasing its computational cost. A stochastic basis reduction method was employed to generate a smaller basis which could be used in lieu of the full PCE basis, resulting in fewer required evaluations of the potentially expensive QoI. These two methods were demonstrated upon three quantities of interest: the pressure coefficient profile of two NACA0012 airfoil simulations (one at high Mach number, one at low) which utilized two different solvers (XFOIL and FLUENT) for high and low fidelity approximations, and the liquid phase concentration of a LIB, wherein high and low fidelity models were generated via mesh refinement of the same solver. It was found in all cases that both methods offered improvement in predicting the mean and variance of a reference solution as compared to a high fidelity solution for an equivalent number of high fidelity samples and generally featured lower variance of these quantities as well.

The weighted ℓ_1 minimization method used *a priori* information about the decay of the PC coefficients of a low fidelity model to promote sparsity in a corresponding high fidelity model. This method relies on the idea that while the actual values of the vector of sparse coefficients of the PCE may differ between high and low fidelity models, their relative contributions and sparsity should be similar. Improvements were observed for both the mean and the variance in the airfoil

problems for low high fidelity samples N^H over the high fidelity approximation. Variance in both the mean and variance was also consistently lower for the bi fidelity approximations than the high fidelity approximations for a given N^H. Improvements in predicting the mean and variance were also observed for the LIB model with low variance seen in both of these quantities. Though the idea of weighting the BPDN algorithm is not new, using the coefficients of a corresponding low fidelity model as the weights represents an original contribution to the UQ field.

It has been shown that an ideal basis for a stochastic QoI can be constructed from the principle component analysis of its covariance matrix, which is formed from a polynomial chaos expansion. Such a basis is truncated according to the (usually rapid) decay of its eigenvalues, i.e., the relative contributions of its nodal modes, and subsequently, can feature significantly fewer terms than the full PC basis. As the PCE and therefore covariance of a high fidelity model may be unavailable, this method cannot be directly applied to a high fidelity model. However, if it is assumed that errors in stochastic space are largely independent of errors in model physics (due to discretization error, physics simplification, etc.), than the PCE of a low fidelity model may be used instead of that of a high fidelity to form the covariance matrix. The resulting basis will be much smaller, and therefore requires significantly fewer evaluations of a high fidelity quantity of interest to fully determine. For an appropriately chosen rank of approximation, it was found that the basis reduction method could offer roughly an order of magnitude improvement in approximating the mean of the reference QoI over the high fidelity model alone for an equivalent number of high fidelity samples. For the entire range of N^H for both the airfoil problems and the LIB simulation, the high fidelity model was never observed to overtake the basis reduction method either in predicting the mean or the variance. The successful implementation of the basis reduction method upon high and low fidelity models that featured two different solvers represents a new contribution to the UQ body of literature.

In summary, this thesis has shown promising results for two new techniques for developing cost effective PCEs for simulated high fidelity quantities of interest.

4.2 Future Work

The methods explored in this manuscript present many avenues for future research. Provided here is a compilation of two potential areas for further development for this topic, organized in ascending order of difficulty.

(1) **Explore optimal sampling of the stochastic reduced basis.** The goal of optimal sampling design is to intelligently select sampling points that will return sharp estimates of parameters, such as PCE coefficients $\boldsymbol{c}$, while minimizing the total number of samples required; the choice of samples is optimal with respect to some statistical criteria, and can include such strategies as A-optimality (which seeks to minimize the trace of the inverse of the information matrix), D-optimality (which seeks to maximize the determinant of the information matrix), and E-optimality (which seeks to maximize the smallest eigenvalue of the information matrix) [37]. Optimal sampling for PCE is a concept that has been explored previously [48], but as the basis reduction method represents a linear transformation of the PCE, it is unclear how this might impact sampling optimality. It is therefore of great interest to investigate how appropriate sampling could further improve the computational efficiency of this method.

(2) **Develop a methodology for determining the quality of low fidelity models.** Both techniques entailed in this thesis relied on the ability of a low fidelity model to accurately reproduce some quality of a high fidelity model, despite yielding an inaccurate approximation of the model overall. In the case of the basis reduction method, the low fidelity model was able to accurately approximate the eigenvalue decay of the covariance of the reference solution. In the weighted ℓ_1 approach, the low fidelity model was able to capture the approximate sparsity of the reference model and relative contributions of its coefficients, thereby promoting accurate sparsity. However, the viability of a low fidelity model for predicting some important quality of a high fidelity model is extremely problem specific, and is still very much an open question in the UQ community. The development of an

analytical framework for assessing the quality of a low fidelity model *a priori* is an essential task that remains unfinished and would be invaluable for multi fidelity methods.

Bibliography

[1] Alen Alexanderian, Oliver P. Le Maître, Habib N. Najm, Mohamed Iskandarani, and Omar M. Knio. Multiscale stochastic preconditioners in non-intrusive spectral projection. Journal of Scientific Computing, 50, 2012.

[2] John Red Horse Alireza Doostan, Roger G. Ghanem. Stochastic model reduction for chaos representations. Computer methods in applied mechanics and engineering, 196:3951 – 3966, 2007.

[3] Pankaj Arora, Ralph E White, and Marc Doyle. Capacity fade mechanisms and side reactions in lithium-ion batteries. Journal of the Electrochemical Society, 145(10):3647–3667, 1998.

[4] R Askey and J Wilson. Some basic hypergeometric polynomials that generalize jacobi polynomials, mem. Amer. Mark. Sot, 318, 1985.

[5] Volker Barthelmann, Erich Novak, and Klaus Ritter. High dimensional polynomial interpolation on sparse grids. Advances in Computational Mathematics, 12(4):273–288, 2000.

[6] Max Gunzburger Benjamin Peherstorfer, Karen Willcox. Survey of multifidelity methods in uncertainty propogation, inference, and optimization. Technical Report TR16-1, ACDL, June 2016.

[7] Marc Berveiller, Bruno Sudret, and Maurice Lemaire. Stochastic finite element: a non intrusive approach by regression. European Journal of Computational Mechanics/Revue Européenne de Mécanique Numérique, 15(1-3):81–92, 2006.

[8] Jeroen AS Witteveenvand Hester Bijl. Modeling arbitrary uncertainties using gram-schmidt polynomial chaos.

[9] Géraud Blatman and Bruno Sudret. An adaptive algorithm to build up sparse polynomial chaos expansions for stochastic finite element analysis. Probabilistic Engineering Mechanics, 25(2):183–197, 2010.

[10] Gerardine G Botte, Venkat R Subramanian, and Ralph E White. Mathematical modeling of secondary lithium batteries. Electrochimica Acta, 45(15):2595–2609, 2000.

[11] John Burkardt, Max Gunzburger, and Hyung-Chun Lee. Pod and cvt-based reduced-order modeling of navier–stokes flows. Computer Methods in Applied Mechanics and Engineering, 196(1):337–355, 2006.

[12] Emmanuel J Candes. The restricted isometry property and its implications for compressed sensing. Comptes Rendus Mathematique, 346(9):589–592, 2008.

[13] Emmanuel J Candès, Justin Romberg, and Terence Tao. Robust uncertainty principles: Exact signal reconstruction from highly incomplete frequency information. IEEE Transactions on information theory, 52(2):489–509, 2006.

[14] Emmanuel J Candes, Justin K Romberg, and Terence Tao. Stable signal recovery from incomplete and inaccurate measurements. Communications on pure and applied mathematics, 59(8):1207–1223, 2006.

[15] Emmanuel J Candes and Terence Tao. Decoding by linear programming. IEEE transactions on information theory, 51(12):4203–4215, 2005.

[16] Emmanuel J Candes and Terence Tao. Near-optimal signal recovery from random projections: Universal encoding strategies? IEEE transactions on information theory, 52(12):5406–5425, 2006.

[17] Emmanuel J Candès and Michael B Wakin. An introduction to compressive sampling. IEEE signal processing magazine, 25(2):21–30, 2008.

[18] Jean-Marc Martinez CEA. Introduction to polynomials chaos with nisp. 2013.

[19] Rick Chartrand and Wotao Yin. Iteratively reweighted algorithms for compressive sensing. In 2008 IEEE International Conference on Acoustics, Speech and Signal Processing, pages 3869–3872. IEEE, 2008.

[20] Scott Shaobing Chen, David L. Donoho, and Michael A. Saunders. Atomic decomposition by basis pursuit. SIAM Review, 43(1):129–159, 2001.

[21] Y-H Chen, C-W Wang, Gao Liu, X-Y Song, VS Battaglia, and Ann Marie Sastry. Selection of conductive additives in li-ion battery cathodes a numerical study. Journal of the Electrochemical Society, 154(10):A978–A986, 2007.

[22] Haiyan Cheng and Adrian Sandu. Collocation least-squares polynomial chaos method. In Proceedings of the 2010 Spring Simulation Multiconference, page 80. Society for Computer Simulation International, 2010.

[23] Paul G. Constantine, Michael S. Eldred, and Eric T. Phipps. Sparse pseudospectral approximation method. Computer Methods in Applied Mechanics and Engineering, 229232, 2012.

[24] Wei Dai and Olgica Milenkovic. Subspace pursuit for compressive sensing: Closing the gap between performance and complexity. Technical report, DTIC Document, 2008.

[25] Bert J Debusschere, Habib N Najm, Philippe P Pébay, Omar M Knio, Roger G Ghanem, and Olivier P Le Maître. Numerical challenges in the use of polynomial chaos representations for stochastic processes. SIAM journal on scientific computing, 26(2):698–719, 2004.

[26] Chris Lacor Dinesh Kumar, Mehrdad Raisee. An efficient non-intrusive reduced bais model for high dimesnioal stochastic problems in cfd. Computers and Fluids, 138:67–82, 2016.

[27] David L Donoho. Compressed sensing. IEEE Transactions on information theory, 52(4):1289–1306, 2006.

[28] David L Donoho. For most large underdetermined systems of linear equations the minimal 1-norm solution is also the sparsest solution. Communications on pure and applied mathematics, 59(6):797–829, 2006.

[29] David L Donoho and Michael Elad. Optimally sparse representation in general (nonorthogonal) dictionaries via 1 minimization. Proceedings of the National Academy of Sciences, 100(5):2197–2202, 2003.

[30] Alireza Doostan and Houman Owhadi. A non-adapted sparse approximation of pdes with stochastic inputs. Journal of Computational Physics, 230(8):3015–3034, 2011.

[31] Marc Doyle, Thomas F Fuller, and John Newman. Modeling of galvanostatic charge and discharge of the lithium/polymer/insertion cell. Journal of the Electrochemical Society, 140(6):1526–1533, 1993.

[32] Mark Drela and Harold Youngren. Xfoil.

[33] Michael Scott Eldred. Recent advances in non-intrusive polynomial chaos and stochastic collocation methods for uncertainty analysis and design. AIAA Paper, 2274(2009):37, 2009.

[34] Michael Scott Eldred, Clayton Garrett Webster, and Paul Constantine. Evaluation of non-intrusive approaches for wiener-askey generalized polynomial chaos. In Proceedings of the 10th AIAA Non-Deterministic Approaches Conference, number AIAA-2008-1892, Schaumburg, IL, volume 117, page 189, 2008.

[35] Stephen P. Boyd Emmanuel J. Candes, Michael B. Wakin. Enhancing sparsity by reweighted l1 minimization. Journal of Fourier Analysis and Applications, 14(5):877–905, December 2008.

[36] O Divorra Escoda, Lorenzo Granai, and Pierre Vandergheynst. On the use of a priori information for sparse signal approximations. IEEE transactions on signal processing, 54(9):3468–3482, 2006.

[37] Valerii V Fedorov and Peter Hackl. Model-oriented design of experiments, volume 125. Springer Science & Business Media, 2012.

[38] GS Fishman and Monte-Carlo Concepts. Algorithms and applications. Springer-Verlag, New York, 1996.

[39] S. Foucart and H. Rauhut. A mathematical introduction to compressive sensing (Applied and numerical harmonic analysis). Springer-Verlag New York, 2013.

[40] Dongdong Ge, Xiaoye Jiang, and Yinyu Ye. A note on the complexity of l p minimization. Mathematical programming, 129(2):285–299, 2011.

[41] Thomas Gerstner and Michael Griebel. Numerical integration using sparse grids. Numerical algorithms, 18(3-4):209–232, 1998.

[42] Thomas Gerstner and Michael Griebel. Dimension–adaptive tensor–product quadrature. Computing, 71(1):65–87, 2003.

[43] Roger Ghanem. Ingredients for a general purpose stochastic finite elements implementation. Computer Methods in Applied Mechanics and Engineering, 168(1):19–34, 1999.

[44] Roger Ghanem. Stochastic finite elements with multiple random non-gaussian properties. Journal of Engineering Mechanics, 125(1):26–40, 1999.

[45] Roger Ghanem and PD Spanos. Polynomial chaos in stochastic finite elements. Journal of Applied Mechanics, 57(1):197–202, 1990.

[46] Roger G Ghanem and Pol D Spanos. Stochastic finite elements: a spectral approach. Courier Corporation, 2003.

[47] Mohammed Hadigol, Kurt Maute, and Alireza Doostan. On uncertainty quantification of lithium-ion batteries: Application to an lic6/licoo2 cell. Journal of Power Sources, 300:507 – 524, 2015.

[48] Jerrad Hampton and Alireza Doostan. Coherence motivated sampling and convergence analysis of least squares polynomial chaos regression. Computer Methods in Applied Mechanics and Engineering, 290:73–97, 2015.

[49] Serhat Hosder, Robert W Walters, and Michael Balch. Efficient sampling for non-intrusive polynomial chaos applications with multiple uncertain input variables. AIAA paper, 1939:2007, 2007.

[50] W.-S. Lu J. K. Pant and A. Antoniou. Reconstruction of sparse signals by minimizing a re-weighted approximate 0-norm in the null space of the measurement matrix. University Lecture, 2010.

[51] Alireza Doostan Jerrad Hampton. Compressive sampling of polynomial chaos expansion: convergence analysis and sampling strategies. Journal of Computational Physics, 280:363 – 386, 2015.

[52] Alireza Doostan Ji Peng, Jerrad Hampton. A weighted l1-minimization approach for sparse polynomial chaos expansions. Journal of Computational Physics, 267:92–111, 2014.

[53] Alireza Doostan Ji Peng, Jerrad Hampton. On polynomial chaos expansion via gradient-enhanced l1-minimization. Journal of Computational Physics, 310:440 – 458, April 2016. l1.

[54] Ian Jolliffe. Principal component analysis. Wiley Online Library, 2002.

[55] Samuel Karlin and James L McGregor. The differential equations of birth-and-death processes, and the stieltjes moment problem. Transactions of the American Mathematical Society, 85(2):489–546, 1957.

[56] Olivier Le Maître and Omar M Knio. Spectral methods for uncertainty quantification: with applications to computational fluid dynamics. Springer Science & Business Media, 2010.

[57] Leifur Leifsson, Slawomir Koziel, Yi Zhang, and Serhat Hosder. Low-cost robust airfoil optimization by variable-fidelity models and stochastic expansions. In 51st AIAA Aerospace Sciences Meeting including the New Horizons Forum and Aerospace Exposition, pages 7–10, 2013.

[58] D Lucor, C Enaux, H Jourdren, and P Sagaut. Stochastic design optimization: Application to reacting flows. Computer Methods in Applied Mechanics and Engineering, 196(49):5047–5062, 2007.

[59] D. xiu Lucor and G. Karniadakis. Spectral representations of uncertainty in simulations: Algorithms and applications. In Proceedings of the International Conference on Spectral and High Order Methods, ICOSAHOM-01, 2001.

[60] Qin Lyu, Zhouchen Lin, Yiyuan She, and Chao Zhang. A comparison of typical p minimization algorithms. Neurocomputing, 119:413–424, 2013.

[61] Lionel Mathelin, M Yousuff Hussaini, and Thomas A Zang. Stochastic approaches to uncertainty quantification in cfd simulations. Numerical Algorithms, 38(1-3):209–236, 2005.

[62] MATLAB. version R2015b. The MathWorks Inc., Natick, Massachusetts, 2015.

[63] J. Burkardt M.S. Eldred. Comparison of non-intrusive polynomial chaos and stocahstic collocation methods for uncertainty quantification. In 47th AIAA Aerospace Sciences Meeting including the New HOrizons Forum and Aerospace Exposition. AIAA, January 2009.

[64] Leo Wai-Tsun Ng and MS Eldred. Multifidelity uncertainty quantification using nonintrusive polynomial chaos and stochastic collocation. In Proceedings of the 14th AIAA Non-Deterministic Approaches Conference, number AIAA-2012-1852, Honolulu, HI, volume 43, 2012.

[65] Leo WT Ng and Karen E Willcox. Multifidelity approaches for optimization under uncertainty. International Journal for Numerical Methods in Engineering, 100(10):746–772, 2014.

[66] Andreas Nyman. An experimental and theoretical study of the mass transport in lithium-ion battery electrolytes. 2011.

[67] Anthony OHagan. Polynomial chaos: A tutorial and critique from a statisticians perspective. SIAM/ASA J. Uncertainty Quantification, 20:1–20, 2013.

[68] A Santiago Padrón, Juan J Alonso, and Michael S Eldred. Multi-fidelity methods in aerodynamic robust optimization. In 18th AIAA Non-Deterministic Approaches Conference, page 0680, 2016.

[69] A Santiago Padrón, Juan J Alonso, Francisco Palacios, Matthew Barone, and Michael S Eldred. Multi-fidelity uncertainty quantification: application to a vertical axis wind turbine under an extreme gust. In 15th AIAA/ISSMO Multidisciplinary Analysis and Optimization Conference, Atlanta, GA, USA, 2014.

[70] Benjamin Peherstorfer, Karen Willcox, and Max Gunzburger. Survey of multifidelity methods in uncertainty propagation, inference, and optimization. Technical report, 2016.

[71] Tiehua Piao, Su-Moon Park, Chil-Hoon Doh, and Seong-In Moon. Intercalation of lithium ions into graphite electrodes studied by ac impedance measurements. Journal of The Electrochemical Society, 146(8):2794–2798, 1999.

[72] David R. Dowling Pijust K. Kundu, Ira M. Cohen. Fluid Mechanics 6th edition. ELSEVIER, 6 edition, 2016.

[73] Gaël Poëtte and Didier Lucor. Non intrusive iterative stochastic spectral representation with application to compressible gas dynamics. Journal of Computational Physics, 231(9):3587–3609, 2012.

[74] Geoffrey Thomas Parks Pramudita SAtria Palar, Takeshi Tsuchiya. Multi-fidelity non-intrusive polynomial chaos based on regression. Comput. Methods Appl. Mech. Engrg, 305:579–606, 2016.

[75] Clarence W Rowley. Model reduction for fluids, using balanced proper orthogonal decomposition. International Journal of Bifurcation and Chaos, 15(03):997–1013, 2005.

[76] Roland Schobi, Bruno Sudret, and Joe Wiart. Polynomial-chaos-based kriging. International Journal for Uncertainty Quantification, 5(2):171–193, 2015.

[77] Harsheel Shah, Serhat Hosder, Slawomir Koziel, Yonatan A Tesfahunegn, and Leifur Leifsson. Multi-fidelity robust aerodynamic design optimization under mixed uncertainty. Aerospace Science and Technology, 45:17–29, 2015.

[78] PR Shearing, LE Howard, Peter Stanley Jørgensen, NP Brandon, and SJ Harris. Characterization of the 3-dimensional microstructure of a graphite negative electrode from a li-ion battery. Electrochemistry communications, 12(3):374–377, 2010.

[79] Sergey A Smolyak. Quadrature and interpolation formulas for tensor products of certain classes of functions. In Dokl. Akad. Nauk SSSR, volume 4, page 123, 1963.

[80] Christian Soize and Roger Ghanem. Physical systems with random uncertainties: chaos representations with arbitrary probability measure. SIAM Journal on Scientific Computing, 26(2):395–410, 2004.

[81] Bruno Sudret. Global sensitivity analysis using polynomial chaos expansions. Reliability Engineering & System Safety, 93(7):964–979, 2008.

[82] Karen E Thomas, John Newman, and Robert M Darling. Mathematical modeling of lithium batteries. In Advances in lithium-ion batteries, pages 345–392. Springer, 2002.

[83] Norbert Wiener. The homogeneous chaos. American Journal of Mathematics, 60(4):897–936, 1938.

[84] Justin Gregory Winokur. Adaptive Sparse Grid approaches to Polynomial Chaos Expansions for Uncertainty Quantification. PhD thesis, Duke, 2015.

[85] Dongbin Xiu and George Em Karniadakis. The wiener–askey polynomial chaos for stochastic differential equations. SIAM Journal on Scientific Computing, 24(2):619–644, 2002.

[86] Dongbin Xiu and George Em Karniadakis. The wiener–askey polynomial chaos for stochastic differential equations. SIAM journal on scientific computing, 24(2):619–644, 2002.

[87] Dongbin Xiu and George Em Karniadakis. Modeling uncertainty in flow simulations via generalized polynomial chaos. Journal of computational physics, 187(1):137–167, 2003.

[88] Xiu Yang and George Em Karniadakis. Reweighted 1 minimization method for stochastic elliptic differential equations. Journal of Computational Physics, 248:87–108, 2013.

[89] Wotao Yin. Sparse optimization; lecture: Sparse recovery guarantees. University Lecture, 2013.

[90] Yi Zhang, Serhat Hosder, Leifur Leifsson, and Slawomir Koziel. Robust airfoil optimization under inherent and model-form uncertainties using stochastic expansions. In 50th AIAA Aerospace Sciences Meeting Including the New Horizons Forum and Aerospace Exposition, pages 2012–0056, 2012.

.1 Determination of δ

In the weighted BPDN method, a small damping parameter δ is added to the weights to ensure stability:

$$w_j = (c_j^L + \delta)^{-1}. \tag{1}$$

Studies have shown the WBPDN algorithms to be somewhat robust to the choice of δ [35], but one possible cross validation method is detailed here for the interested reader. Setting δ to be a fraction of the largest low fidelity coefficient, $max(c_j^L)$, sets a threshold that is reasonable to the magnitude of the problem at hand:

$$\delta = \delta_w \max(\boldsymbol{c}^L). \tag{2}$$

A cross validation study was performed upon a lower dimension airfoil simulation. Two random inputs were used: $M \sim U(.1, .3)$ and $\alpha \sim U(8, 12)$ degrees. As in the 6d airfoil analysis, the 2d airfoil was simulated using XFOIL (the low fidelity solver) and FLUENT (the high fidelity solver) as a function of the two random inputs. A reference PCE was formed using all available high fidelity samples. δ_w was varied between $\delta_w = 1e-2, 1e-4$ and the multi fidelity WBPDN method was performed at each δ_w for a limited number of high fidelity samples. The relative error between the bi fidelity coefficients and the reference coefficients was then examined for 100 ensembles of N^H and averaged. As can be seen in Fig. 1, very little difference could be observed in the errors, so $\delta_w = 1e-3$ was selected for all subsequent analyses. Computational resources did not allow for the generation of an additional lower dimensional lithium ion battery simulation, so δ_w was selected to be $1e-3$ for all LIB analyses as well.

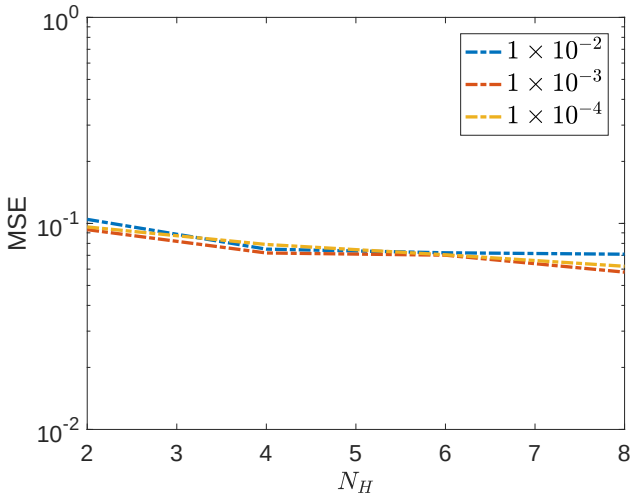

Figure 1: Study of δ_w using lower dimensional stochastic airfoil model.